

The role of chemical, polar and octahedral tilt disorder in high voltage/energy density ceramics

Ian M. Reaney¹, Richard Beanland², Robin Sjökvist² , Yubo Zhu¹, Ge Wang³  and Derek C. Sinclair¹

Abstract

Power modules in electric vehicles (EVs) are essential electronic components that manage and convert electrical power between the battery and other vehicle systems, such as the motor. The electronics are required to operate at higher temperatures ($>200\text{ }^{\circ}\text{C}$) and fields ($>0.5\text{ MV/cm}$) than in conventional consumer goods such as phones and tablets. This requires the use of, e.g., SiC based semiconductor technology, along with associated filters/capacitors that can withstand high temperature/fields. Such capacitors have a large energy density arising from the ability of the dielectric to withstand repeated application of high fields ($>0.5\text{ MV/cm}$) without breakdown. This article reviews examples and presents new data and concepts on high energy density dielectrics intended for use in power electronic. In particular, the article focuses on a new class of dielectrics which have high permittivity (>1000) but do not saturate at high field and exhibit a quasi-linear polarisation-field response. The roles of chemical, polar and octahedral tilt disorder are assessed and a new mechanism proposed by which tilt disorder restricts strain coupling and therefore polar coupling, leading to a quasi-linear response in polarisation-field (P-E) loops. The influences of local variations in stoichiometry and multi-valent and multi-sized substituents in these polar lattices to attain enhanced resistivity are also discussed. The article therefore illustrates how a combination of high resistivity and tilt disorder are pivotal in the design of a new generation of high energy density capacitors for power electronics.

Keywords

dielectrics, disorders, polar coupling, quasi-linear, high voltage/energy density capacitors

Received: 16 June 2025; accepted: 26 November 2025

Introduction

Power electronics will play a central role in the impending energy transition from fossil fuels to electrification, which will profoundly change transport and energy distribution infrastructure. New wide-bandgap semiconductor technologies provide active components that can operate at $200\text{ }^{\circ}\text{C}$ or above, allowing reductions in heatsink size and equipment weight.¹ However, the high switching speeds of these wide-bandgap devices require that passive and active components must be in close proximity (i.e., co-packaged), demanding high temperature operation of the passive components. The development of next generation Class-II dielectrics with a wide operating temperature range, from -55 to $200\text{--}300\text{ }^{\circ}\text{C}$ (operating window for power electronics), is thus of global importance. In addition, they must work at higher operating fields ($>500\text{ kV/cm}$), be Pb-free and not prohibitively expensive to manufacture, i.e., compatible with base metal electrodes (BME) such as Ni.

Over the last decade many attempts have been made to replace BaTiO₃, the dominant dielectric in the manufacture of multilayer ceramic capacitors (MLCCs) in consumer electronics, for one better suited to power electronics. The breakdown strength and operating temperature of classic X7R

BaTiO₃-based dielectrics are too low and the dielectric ‘tunes’ at high field, limiting the permittivity to ~ 300 rather than 2000 at low field. To date, high permittivity compositions such as Bi-based relaxors (REL)² and various anti-ferroelectric (AFE)³ compositions have been proposed but they are either incompatible with low-cost electrodes (Bi reacts with Ag-0.1Pd and Ni) and/or exhibit large strains leading to mechanical failure due to either a field induced transition from AFE to FE or REL to FE. As a result, the default mode in power electronics is currently CaZrO₃ based dielectrics whose volumetric efficiency is low due to their low permittivity ($\epsilon_r \sim 30$).⁴

Much emphasis in the field of high voltage capacitors has been placed on recovery/discharge energy density (W_{rec} ,

¹School of Chemical, Materials and Biological Engineering, Functional Materials and Devices Group, University of Sheffield, Sheffield, UK

²Department of Physics, University of Warwick, Coventry, UK

³Department of Materials, University of Manchester, Manchester, UK

Corresponding author:

Ge Wang, Department of Materials, University of Manchester, Oxford Road, Manchester, M13 9PL, UK.
Email: ge.wang@manchester.ac.uk

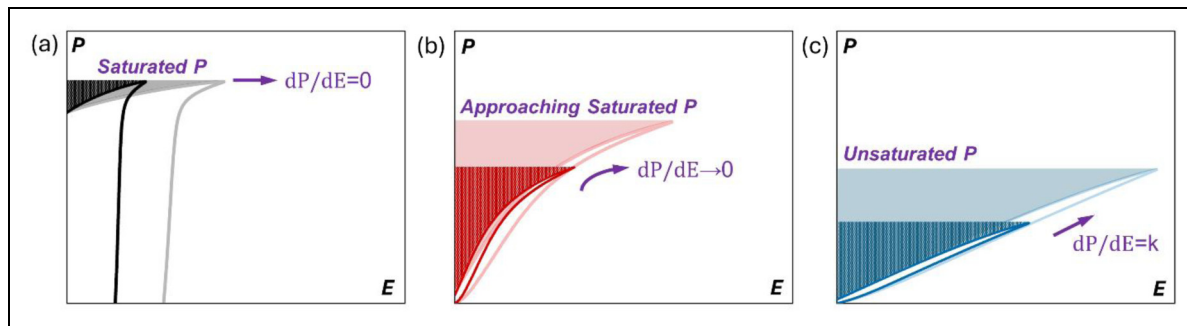


Figure 1. Schematic of unipolar P-E loops of different dielectrics for electrostatic energy storage: a) ferroelectric ($dP/dE = 0$); b) relaxor ferroelectric ($dP/dE \rightarrow 0$) and c) quasi-linear dielectrics ($dP/dE = \text{constant, } k$).

given by the area to the left of a unipolar P-E curve (shaded areas in Figure 1).^{2,3} W_{rec} is an excellent ‘Figure of Merit’ to compare materials for power electronic applications, particularly if the P-E loops are obtained as a function of temperature since high maximum electric field (E_{max}) necessitates high breakdown strength and $dP/dE = \epsilon$.^{2,3} Figure 1(a) illustrates a FE response in which $dP/dE = 0$ at high field (tunes). Figure 1(b) is from a relaxor (REL) in which $dP/dE \rightarrow 0$, i.e., the dielectric still tunes and permittivity reduces at high field but not to the extent of FE materials. Figure 1(c) is an example of a linear (or quasi-linear) dielectric (QLD) in which dP/dE is effectively constant (k) and does not tune. QLDs differ from conventional linear dielectrics in that they have considerably higher ϵ_r (>600) as opposed to 10 for alumina⁵ or 30 for CaZrO_3 .⁴ Such large values of ϵ_r with virtually linear P-E response is until recently unknown. We propose therefore that an ideal dielectric for high field applications should not tune ($dP/dE = k$), have a high ϵ_r (>500) and should not significantly deviate from its room temperature characteristics above 200 °C (temperature stable). The area enclosed by the P-E loops in Figure 1 approximates to high field loss (W_{loss}) and gives the efficiency (η) of the dielectric during discharge as $W_{\text{rec}}/(W_{\text{rec}} + W_{\text{loss}})$. Opening of the loop, relates to the switching of domains and/or the movement of defects (i.e., ionic and/or electronic conduction) under the applied field. Both are a source of dielectric loss in the system and can lead to self-heating of the MLCC. η therefore is an ideal ‘Figure of Merit’ to assess the high field loss and should be close to 100% for MLCCs for power electronics.²

There are a number of AFE systems, mainly based on NaNbO_3 (NN) and AgNbO_3 (AN) which have been explored for pulsed power application.³ They have a high energy density but for high voltage capacitors a sudden step change in permittivity at the field induced transition, prohibits their use in power electronics. Instead, relaxor or paraelectric systems are preferred in which the change in ϵ_r as a function of field and temperature is more predictable.^{6–12} Empirically, the importance of chemical disorder in the development of high voltage dielectric relaxor-ferroelectric and paraelectric ceramics is well established.^{6–12} Many authors now choose to express perovskite compositions using a single ABO_3 formula, i.e., with multiple A- and B-site ions, rather than as ternary or quaternary solid solutions, thereby emphasising the ‘high entropy’ within the composition.^{13,14} High entropy oxides consist of five or more metallic elements in near-

equimolar proportions, forming a single-phase solid solution. The high configurational entropy is said to stabilise these materials in either non-equilibrium crystal structures and/or imparts them with novel properties.¹⁵ There is no strong evidence of stabilisation of non-equilibrium structures within high voltage/energy dielectrics since all materials form conventional solid solutions.^{16,17} In some cases however, end members are introduced into the solid solution which do not in themselves form a stable perovskite structure, such as $\text{BiMg}_{2/3}\text{Nb}_{1/3}\text{O}_3$ in $\text{BaTiO}_3 - \text{BiFeO}_3 - \text{BiMg}_{2/3}\text{Nb}_{1/3}\text{O}_3$.^{18,19} Whilst it can be argued that $\text{BiMg}_{2/3}\text{Nb}_{1/3}\text{O}_3$ is ‘entropy stabilised’, equally Mg^{2+} and Nb^{5+} may be viewed as entering into solid solution as ionically compensated dopants, an effect that has been known for number of years. More fundamentally, considerations of entropy constitute a phenomenological approach dealing with macroscopic properties which by definition do not engender a microscopic or mechanistic understanding. It should also be noted that the materials described in ref Wang et al.²⁰ are composed of ~80% NN and do not conform to any definition commonly used for high entropy dielectrics yet exhibit some of the highest values of W_{rec} reported to date for MLCCs.

Nonetheless, it is evident that increasing the number of different A- and B-site species within systems that contain highly polarisable cations such as Bi, Nb, Ti and Pb reduces polar order, forcing a relaxor or paraelectric state.^{6–12} The distribution of valence states/ion-size throughout the A and B-sites contributes to a high breakdown strength, despite no macroscopic driving force for the formation of defects since they are substituted into the lattice with the appropriate ionic compensation, i.e., they are stoichiometric substituents.^{6–12} However, non-stoichiometric defects may form locally which are compensated over larger volumes, creating a short range ordered multi-defect state that appears critical for optimising breakdown strength and by default energy density. *In this article, we will describe examples of the stoichiometric alloying effect and postulate about the possible mechanisms by which resistivity is enhanced.*

Almost all papers, consider chemical and polar disorder as factors that contribute to the design of high voltage/energy density dielectric ceramics.^{6–12} Only a few in contrast, consider the role of distortions of the BO_3 octahedral framework, despite the largest energy densities and break down strengths in perovskite structured dielectrics being associated with octahedral tilted or short range tilted systems.^{20,21} Moreover, the recent demonstration of large energy densities in a tetragonal

tungsten bronze (TTB) structured ferroics whose octahedral tilt structure forms a frustrated incommensurate lattice,²² reinforces the view that *octahedral tilt disorder is pivotal in designing ceramics for high voltage/energy density applications*.

Role of doping/alloying in the control of electrical properties

A) Intrinsic resistivity and breakdown strength

The two main factors that influence insulation resistance (IR) and breakdown strength (BDS) are the (physical) ceramic and electrical microstructure of the dielectric body, which may or may not be the same. The physical microstructure can contain many different features, for example, a distribution of grain sizes and shapes and level/shape/distribution of porosity, inter-grain boundary regions of different thickness and/or composition, intra-grain regions based on core and shell regions and/or surface layers on the 'skin' of the ceramics with different composition and/or distribution of defects such as oxygen vacancies. Each of these regions (if present) can have their own electrical properties (e.g., values of permittivity and conductivity) and depending on their relative values can influence the measured electrical properties. The electrical microstructure is based on how the current is transported through these various electro-active regions (for IR) and how the electric field is supported within the ceramic (for BDS).

In general, most researchers use only low field measurements to assess IR of ceramics via methods such as Impedance Spectroscopy (IS), where a low ac signal, typically 100 mV across a wide frequency range (e.g., 10^{-2} to 10^6 Hz) is applied across a sample that is 1–2 mm thick with symmetric (top and bottom) electrodes.²³ In contrast BDS on the same samples is often estimated from P-E measurements where much higher ac fields, e.g., >300 kV/cm are applied at a selected frequency, e.g., 1 Hz.² These are very different measurements and provide different but complimentary information on the electrical microstructure and properties, notwithstanding that the electrical properties of many of these regions may exhibit non-ohmic (i.e., voltage dependent) behaviour. Furthermore, to test ceramics at higher fields and avoid arcing (or air breakdown) around the sample, it has become common practice in P-E measurements to employ a smaller-area top electrode paired with a full bottom electrode.²⁴ For small top-electrode areas, this configuration can generate significant non-uniformity and extremely high electric fields, along with spreading resistance effects near the top contact. Such issues distort P-E loop shapes (and thus the extracted values for W_{rec} , W_{loss} and η), as well as BDS estimates.²⁴ For example, in BaTiO₃ ceramics, increasing the thickness-to-top-electrode radius ratio (S/r) from 0.17 to 1.96 broadens and distorts loops, raising W_{rec} by approximately 1.4 times and drops η from 29 to 8%. These effects arise from geometric confinement and electrode interference, leading to underestimation of the local field at high S/r values. To promote reproducibility and fair comparisons, researchers should report electrode areas, sample thicknesses, and S/r ratios alongside P-E data.

Although no universal standard exists, it is advisable to use top and bottom electrodes of equal area (covering > 80% of the sample surface) for bulk ceramics, thereby minimising field non-uniformity and approximating full top-bottom configurations. Equally important is correcting for thickness effects; thus, good metrology demands disclosure of both electrode areas and sample thickness in P-E studies. Normalisation offers an effective way to mitigate thickness- and area-related biases. Thinner samples (< 0.2 mm) can boost E_{max} up to four-fold through defect reduction, while smaller areas (< 1 cm²) roughly double ΔP (and hence W_{rec}), as reported by Wang *et al.*²⁵ It is recommended to normalise energy-storage performance using thickness-independent metrics such as $W_n = W_{rec}/E_{max}$ and area-independent ones such as $W_n = W_{rec}/\Delta P$, enabling cross-format comparisons across bulk, multilayer, and thin-film systems.

In the case of IS, it is often possible to assess (at least at low electric fields) the IR electrical properties of different electro-active regions, whereas for P-E measurements this is not possible as the area within the loops contains contributions from dipoles through domain switching, and conduction though e.g., the migration of oxygen vacancies with samples.

The brickwork layer model (BLM) is often used to analyse IS data of electroceramics and works well when the grain boundary regions are more resistive than the grains (bulk), i.e. $R_{gb} \gg R_b$, levels of porosity are low (< 5 vol%) and there is a uniform grain structure.²² In this model, the current pathway is assumed to be a simple series connection of these electroactive regions and the total (IR) resistance is $R_b + R_{gb}$. Thus, to maximise IR, it is advantageous to have small grains to ensure a high-volume fraction of grain boundaries and to minimise porosity to avoid arcing within the ceramic that can lead to low BDS during P-E measurements. If the grains contain a core-shell microstructure, then providing $R_{shell} \gg R_{core}$ the BLM is still applicable and the total resistance of the ceramic is $R_{core} + R_{shell} + R_{gb}$.^{23,26} The electrical homogeneity of the grains is best probed by analysing the complex electric modulus formalism (M^*) which is sensitive to small (and therefore bulk-type) capacitances. The total resistance of the ceramics is best analysed by the complex impedance formalism (Z^*) which is dominated by the most resistive regions which is typically the grain boundaries, if they are electro-active. Combined $-Z''$ and M'' spectra are therefore often a convenient way to present IS data to visually assess the electrical homogeneity of electroceramics.^{23,26}

B) Defect chemistry in ferroics

Most ferroic perovskite and TTB materials are based on B-site d⁰ cations, i.e., BaTiO₃, Pb(Zr,Ti)O₃, NaNbO₃, (Na_{1/2}Bi_{1/2})TiO₃ and (Ba,Sr)Nb₂O₆. They exhibit wide band gaps (> 3 eV) and are therefore a natural choice as dielectric materials since their intrinsic conductivity (i.e., conduction across the band gap between a filled valence band and empty conduction band) should remain low until high temperatures. One exception is BiFeO₃ which is based on Fe³⁺ (d⁵) with a band gap of 2.8 eV but this remains sufficient to adequately assess the dielectric behaviour. Due to their low levels of intrinsic conduction near room temperature (RT), the leakage conduction mechanism(s) are either predominantly extrinsic

due to aliovalent impurities (i.e., donors or acceptors) and/or due to non-stoichiometry associated with a significant deviation from A/B = 1 in nominally stoichiometric ABO_3 perovskites. This A/B non-stoichiometry may exist intrinsically in the material and/or be induced by ceramic processing. Examples are given below to illustrate how unintentional impurities (BaTiO_3), small variations in A/B ratios ($(\text{Na}_{1/2}\text{Bi}_{1/2})\text{TiO}_3$) and loss of Bi_2O_3 (BiFeO_3) during processing can dominate the conduction properties in single perovskites, precursor to considering the binary/ternary/quaternary systems in high energy density applications.

BaTiO₃, BT, ceramics processed in air typically exhibit extrinsic p-type conduction (i.e., electronic holes) due to the presence of low levels (δ) of trivalent acceptor impurities (predominantly Fe^{3+}) associated with the TiO_2 reagents used to prepare the ceramics.²⁷ The level of impurities creates defect concentrations that exceed those obtained by any non-stoichiometry associated with A/B \neq 1 and therefore dominate the conduction. The impurities arise because synthetic TiO_2 commonly used as a reagent is obtained from the mineral ore Ilmenite, FeTiO_3 . If Fe is present in the starting TiO_2 reagent, the material is nominally cation stoichiometric but is oxygen substoichiometric (based on ideal ABO_3) and should be written as $\text{Ba}(\text{Ti}_{1-\delta}\text{Fe}_\delta)\text{O}_{3-\delta/2}$. When sintered in air, such BT ceramics can gain oxygen from the atmosphere on cooling to (at least partially) fill the oxygen vacancies created by the acceptor impurities, as follows based on Kroger-Vink notation



Electrons are required to form the O^{2-} ions and therefore holes are created in the valence band (or as O^- as opposed to O^{2-} ions in the lattice²⁸) and low levels of p-type conduction arise. The residual oxygen vacancies are not the predominant source of conduction under low electric fields but are a source of oxide-ion (ionic) conduction under high electric fields where ion migration can be appreciable.²⁹ For high field dielectric applications, the presence of oxygen vacancies are detrimental to material performance and their concentration should be minimised.

(Na_{1/2}Bi_{1/2})TiO₃, NBT, has been explored for many decades as a Pb-free piezoelectric material; however, we discovered high levels of oxide-ion conductivity in undoped-NBT that is intimately linked to low levels of A-site non-stoichiometry away from $\text{Na}_{1/2}\text{Bi}_{1/2}$.³⁰ The defect chemistry and high levels of oxygen ion mobility and oxide-ion conduction of NBT is rather different from other well-known perovskite titanates such as BT. These are attributed to changes in the crystal structure (octahedral tilting), the presence of the highly polarisable Bi^{3+} ($6s^26p^0$) ion with its electron lone pair and weak Bi-O bonds.³¹⁻³³

Low levels of A-site non-stoichiometry can be induced by changing the Na/Bi ratio in the nominal starting composition and/or by volatilisation of Bi_2O_3 during ceramic processing of nominally stoichiometric NBT.^{30,32} The level of Bi_2O_3 volatilisation is influenced by the polymorphic form of the TiO_2 reagent (anatase or rutile) used in the solid-state reaction method. The former is more effective in suppressing Bi_2O_3 loss by forming sillenite $\text{Bi}_{12}\text{TiO}_{20}$ prior to forming perovskite NBT.³⁴ In this way, nominally stoichiometric NBT prepared using anatase is an excellent dielectric which

remains electrically insulating with bulk conductivity, $\sigma \sim 2$ mS/cm (at 600 °C) with an activation energy for bulk conduction of 1.7 eV (approximately half the band gap). In contrast, significant Bi_2O_3 loss occurs when using rutile as there is no formation of Bi-rich precursor phase(s) at lower temperature prior to perovskite NBT and this generates A-site and oxygen vacancies during ceramic processing according to the following equation



This gives rise to bulk (grain) oxide-ion conductivity that is 3 orders of magnitude higher at 600 °C with an activation energy of < 0.5 eV.³⁴ This is another example of the important influence that starting reagents (structure and purity) can have in controlling the resulting electrical properties of the target material. It also demonstrates how challenging it can be to achieve the desired electrical properties in ceramics prepared by solid state reactions when low levels (commonly < 1 at%) of impurities and/or non-stoichiometry can have such dramatic effects.

Studies (using rutile TiO_2) have confirmed the Na/Bi starting ratio plays a significant role in the electrical properties and to be a reliable method to ensure either dielectric or oxide-ion (electrolyte) behaviour in NBT. Nominal non-stoichiometry was induced by preparing both Bi- and Na-excess/deficient NBT materials, *viz* $\text{Na}_{1/2}\text{Bi}_{1/2+x}\text{TiO}_3 + 1.5-x/2$ ($x = -0.01$, $\text{NB}_{0.49}$ and $+0.01$, $\text{NB}_{0.51}$) and $\text{Na}_{1/2+y}\text{Bi}_{1/2}\text{TiO}_3 + 0.5y$ ($y = -0.01$, $\text{N}_{0.49}\text{B}$ and $+0.01$, $\text{N}_{0.51}\text{B}$), respectively. In cases where $\text{Na/Bi} < 1$ ($\text{NB}_{0.51}$ and $\text{N}_{0.49}\text{B}$) dielectric behaviour was observed, whereas for $\text{Na/Bi} > 1$ ($\text{NB}_{0.49}$ and $\text{N}_{0.51}\text{B}$) electrolyte behaviour was obtained, Figure 2(a).³⁴ Full explanations of these different types of un-doped behaviour can be found elsewhere²⁹; however, it is important to appreciate that oxide-ion conduction in NBT (and other perovskites) occurs by a hopping mechanism via a saddle point (or bottle neck) between two A-site cations and a B-site cation.

The activation energy, E_a for the oxide ion conduction in NBT (where the Na and Bi ions are disordered on the A-sites) is extremely sensitive to the local bonding of oxygen with the surrounding cations and has been calculated to vary from ~ 0.22 eV where both A-site ions are Bi ions to > 1.0 eV when both are Na ions, Figure 3.³³ The experimental E_a values are closer to the intermediate case of mixed Na/Bi occupation which is in broad agreement with average (disordered A site) crystal structure. This example, where Bi and Na are nominally the same size yet large differences in E_a occur, illustrates that simple crystallochemical considerations such as size (and therefore) strain may not always explain variations in oxide ion conductivity in perovskites.^{36,37} In the case of NBT, other considerations such as the weaker bond strength of Bi to O compared to Na and its higher polarizability are important factors. The local arrangement of the A and B site cations in perovskites and their influence on any oxide-ion conductivity is therefore a combination of multiple contributing factors.

‘Classic’ acceptor and donor doping strategies can be used to enhance or suppress the oxide-ion conductivity in undoped NBT. In these cases, ionic compensation (as opposed to electronic defects) is more favourable and several options are

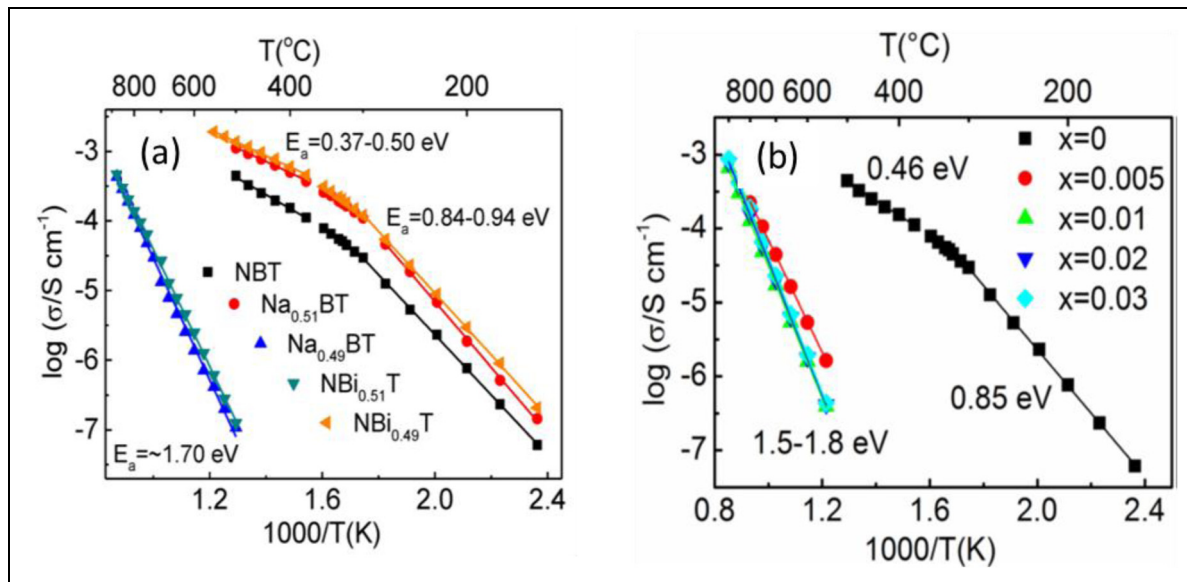


Figure 2. The influence of A-site nominal starting composition (a) and B-site Nb donor doping on the bulk conductivity of NBT (b). Figures adapted from ref Li et al.³⁰ and ref Li et al.³⁴, respectively.

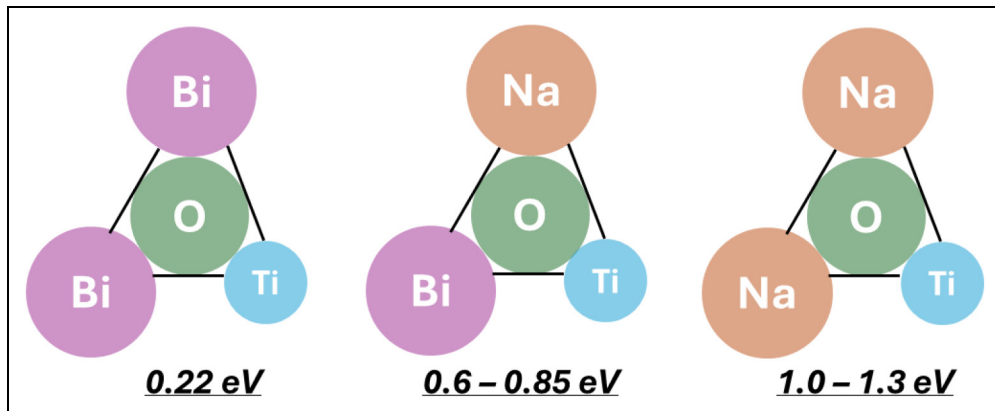
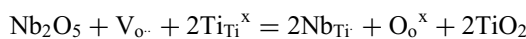


Figure 3. Activation energy for A/B site combinations in NBT. Figures and values adapted from ref Yang et al.³², Yang et al.³³ and He and Mo³⁵.

available.³² For example, either A or B-site acceptor doping with low levels of Sr^{2+} for Bi^{3+} and Mg^{2+} for Ti^{4+} , respectively can increase the level of oxygen vacancies via the following equations and enhance the oxide ion conductivity



In contrast donor doping with Nb^{5+} for Ti^{4+} can be effective in filling oxygen vacancies and switch oxide-ion conducting undoped NBT into an excellent dielectric material, Figure 2(b).³⁸



BiFeO₃, BF. So far our examples have been based on perovskite titanates processed in air and containing Ti^{4+} (d^0). In other ferroic perovskites such as BiFeO₃, Fe can exist in multiple oxidation states, e.g., Fe^{2+} (d^6), Fe^{3+} (d^5) and Fe^{4+} (d^4) and this can further influence the electrical properties, as co-existence of multiple oxidation states of Fe can give rise to appreciable levels of p-type ($\text{Fe}^{3+}/\text{Fe}^{4+}$) electronic

conduction as a consequence of oxidation (oxygen-gain) or n-type ($\text{Fe}^{3+}/\text{Fe}^{2+}$) electronic conduction due to reduction (oxygen-loss). In the case of undoped BiFeO₃, Bi_2O_3 loss is again an issue with high temperature ceramic processing and oxygen gain readily occurs on cooling; however, in this case some of the Fe^{3+} ions are oxidised to Fe^{4+} and this gives rise to appreciable levels of p-type electronic conductivity with a low activation energy of ~ 0.2 eV.^{6,37,39} This is why undoped BiFeO₃ is often quoted as being a ‘leaky’ semiconductor. The leakage electronic conductivity can be avoided by either processing in an inert atmosphere (to avoid oxidation) or by B-site donor doping with Nb^{5+} to fill the oxygen vacancies⁶ as discussed above for NBT. It is important to note that although the conductivity of undoped BiFeO₃ processed in air is dominated by p-type electronic conduction, the re-oxidation process is not complete and oxygen vacancies remain. Although their contribution to the measured bulk conductivity (in air) by IS is low, they can have a significant influence of the electric properties at high electric fields where oxide ion migration can be significant. Furthermore, Alkaline earth doping of Ca, Sr and Ba for Bi

have been shown to create oxygen vacancies (i. $\text{Bi}^{3+} + \frac{1}{2}\text{O}^{\cdot-} \rightarrow \text{Sr}^{2+}$) and this can significantly increase the level of oxide-ion conduction in BiFeO_3 -based ceramics.^{37,39}

Thus far, only single dopants have been considered where the choice of appropriate aliovalent dopants is well established as an effective way to optimise the electrical performance. This minimises IR and therefore promotes the higher BDS required for high energy density applications. However, most materials that are being developed are not based on single materials but are solid solutions of binary/ternary/quaternary systems based on various nominally stoichiometric perovskites. These are commonly a combination of I-V, II-IV and III-III-type ABO_3 , e.g., $\text{NaNbO}_3\text{-SrTiO}_3\text{-La}(\text{Mg}_{1/2}\text{Ti}_{1/2})\text{O}_3$. Although nominally stoichiometric, local variations in stoichiometry may occur (due to $\text{A}/\text{B} \neq 1$) and properties vary/fluctuate (due to donor- and/or acceptor-rich regions) on a submicron level. Achieving chemical (and therefore electrical) homogeneity in such multi-cation-rich perovskites is not trivial given the different diffusion kinetics (and volatility) of the various cations involved and their ability to act as possible donor and/or acceptor dopants.

A simple but illustrative example is that of nominally compensated, acceptor-donor doping of TiO_2 by couples such as $\text{In}^{3+}\text{-Nb}^{5+}$ and $\text{Ga}^{3+}\text{-Nb}^{5+}$ at low dopant levels, i.e., $[(\text{Ga or In})_{1/2}\text{Nb}_{1/2}]_x\text{Ti}_{1-x}\text{O}_2$ with $x \leq 0.10$. These materials attracted attention as apparent colossal permittivity materials with temperature- and frequency-independent permittivity $> 10^4$ and dielectric loss < 0.1 from ~ 50 to 450 K. This behaviour was initially attributed to electron-pinned defect dipoles at low dopant concentrations⁴⁰ however, subsequent studies demonstrated a much simpler explanation associated with electrical heterogeneity in the material due to the challenges associated with controlling the precise acceptor-donor stoichiometry at these low (< 10 at%) doping levels during the growth of single crystals⁴¹ and ceramic processing.⁴² Due to the higher volatility of Ga and In acceptor dopants, low levels of non-stoichiometry in the Nb-acceptor couple develop due to loss of Ga and In and the excess donors are electronically compensated by partial reduction of Ti^{4+} (d^0) to Ti^{3+} (d^1) which induces n-type (electronic) semiconductivity in the grains. The grain boundaries and/or surface layers in the ceramics are electrically more resistive and this results in the development of Schottky barriers at grain boundaries and/or surface layer-electrode (non-ohmic) contacts. These mechanisms and apparent colossal permittivity are similar to that reported in $\text{CaCu}_3\text{Ti}_4\text{O}_{12}$.⁴³⁻⁴⁵

From an electrical perspective it is important that electrical homogeneity is obtained to ensure high IR (or low conductivity) and BDS is obtained in these multicomponent perovskites and TTBs. IS can be a useful probe, at least on a micron level, to ensure the electrical microstructure is sufficiently homogeneous in such ceramics without knowing the precise distributions of the various cations. We illustrate this via three examples.

C) Worked examples of doping/alloying to enhance resistivity

$0.6\text{BiFeO}_3\text{-}0.4\text{SrTiO}_3\text{-}x\text{Nb}$ where $x = 0.00, 0.01, 0.03$ ⁶. The first example is the influence of Nb_2O_5 additions on

$0.6\text{BiFeO}_3\text{-}0.4\text{SrTiO}_3$ ceramics. Without any addition of Nb_2O_5 , the ceramics are leaky semiconductors due to the issues discussed above for BiFeO_3 , and a measurable IS response can be obtained from room temperature, RT. Based on Z^* plots, $x = 0.00$ ceramics have a total resistivity of ~ 180 $\text{k}\Omega\text{cm}$ at RT, Figure 4(a). The corresponding combined $-Z''$ and M'' spectroscopic plots both display two broad and overlapping peaks with the largest peaks in the $-Z''$ and M'' peaks separated by ~ 2 orders of magnitude on a log frequency scale, Figure 4(b). This indicates at least two electroactive components and therefore electrical heterogeneity in $x = 0.00$ ceramics. In contrast, $x = 0.01$ and 0.03 are electrically insulating at RT and useful IS data can only be obtained > 400 °C. Z^* plots at 430 °C show a single arc with total resistivity of ~ 40 to 60 $\text{k}\Omega\text{cm}$, Figure 4(a) and the corresponding combined $-Z''$, M'' spectra (of $x = 0.01$ Nb addition) to contain a single, near-ideal Debye peak that overlap on a log f scale, Figure 4(c). This indicates a single electroactive response and is consistent with a homogeneous electrical microstructure. In most circumstances, the largest M'' peak corresponds to a bulk (grain) dominated response and an Arrhenius plot of conductivity based on this analysis for all these ceramics is shown in Figure 4(d). There is a dramatic change in both the magnitude and activation energy of the bulk conductivity with the addition of Nb_2O_5 . It changes from being ~ 5.5 $\mu\text{S}/\text{cm}$ at RT for $x = 0.00$ to ~ 1 $\mu\text{S}/\text{cm}$ at 350 °C with an increase in E_a from ~ 0.4 to 1.2 eV. This is consistent with a switch from p-type semiconductivity associated with mixed $\text{Fe}^{3+}/\text{Fe}^{4+}$ in $x = 0.00$ towards something that is closer to intrinsic-type conduction which is beneficial for both IR and BDS.

$(0.7 - x)\text{BiFeO}_3\text{-}0.3\text{BaTiO}_3\text{-}x\text{Bi}(\text{Li}_{1/2}\text{Nb}_{1/2})\text{O}_3$ for $x \leq 0.13$ ⁷. The second example is the influence of a ternary compound $\text{Bi}(\text{Li}_{1/2}\text{Nb}_{1/2})\text{O}_3$ (BLN) on a heterogeneous electrical microstructure within the binary system $0.7\text{BiFeO}_3\text{-}0.3\text{BaTiO}_3$. In this case, the ternary compound improves the electrical homogeneity which improves the BDS but has negligible influence on the IR of the ceramics, Figure 5. Based on the single, large $-Z''$ peak that is present at lower frequency with a magnitude between $2\text{-}3$ $\text{M}\Omega\text{cm}$ for all values of x , the total resistivity ($\sim 2Z''_{\text{max}}$) of all the ceramics at 250 °C is $\sim 4\text{M}\Omega\text{cm}$. In this case, the ternary compound BLN does not significantly increase the IR of the ceramics. The presence of two electrically active components in $x = 0.00$ is again apparent based on the M'' spectra and confirms the binary ceramic to be electrically heterogeneous, Figure 5(a). This is confirmed by the modest BDS of < 120 kV/cm for these ceramics. The smaller (higher frequency) M'' peak remains present and clearly visible in the spectra for $x \leq 0.05$, Figure 5(b) but above this its presence is small and for $x = 0.13$ is negligible, Figure 5(c) and (d). The BDS increases systematically from ~ 180 kV/cm for $x = 0.05$ to ~ 260 kV/cm for $x = 0.13$ (optimised material), Figure 5(e). This demonstrates the influence of the ternary compound in improving the electrical homogeneity which in turn improves the BDS. The increase in BDS with the ternary compound may initially be linked (in part) to a reduction in grain size for $x \leq 0.05$ where the average grain size reduces from ~ 8 μm ($x = 0.00$) to ~ 1 μm ($x = 0.05$). However, the systematic change in BDS for $x > 0.05$ is not linked to any changes in grain size where the average

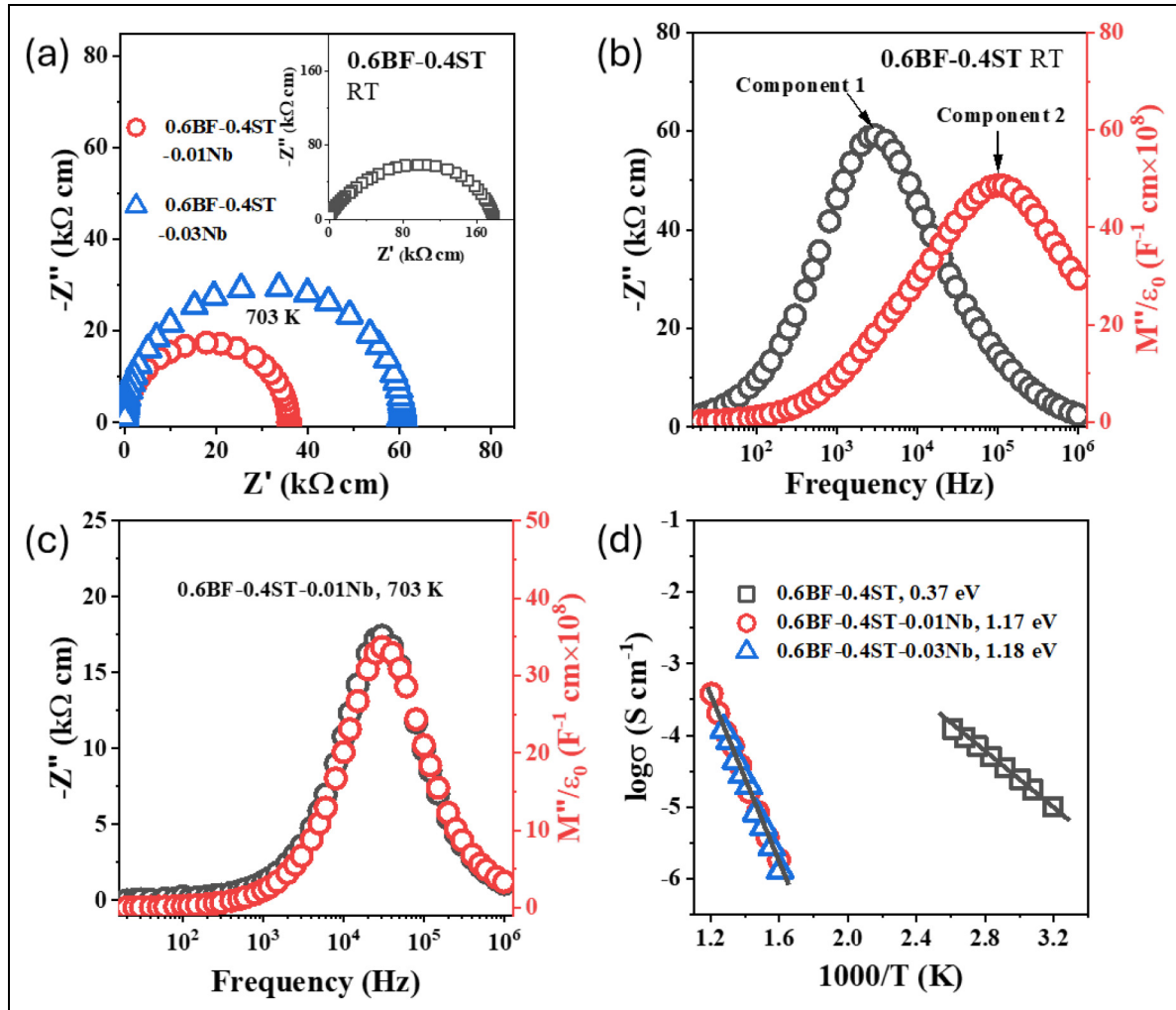


Figure 4. Z^* plots, $-Z''$, M'' spectra and Arrhenius plots of bulk conductivity for various 0.6BF-0.4ST ceramics with and without additions of Nb_2O_5 . Z^* plot for 0.6BF-0.4ST (RT), 0.01 (703 K) and 0.03 (703 K) Nb additions. $-Z''$, M'' spectra for (b) 0.6BF-0.4ST ceramics at RT and (c) 0.01 Nb additions at 703 K. (d) Arrhenius plots of bulk conductivity extracted from M'' spectra. Figure reproduced from ref Lu et al.⁶.

size remains between ~ 1 and $2 \mu\text{m}$. Possible mechanisms for this behaviour are given in the discussion section.

$(0.9-x)\text{NaNbO}_3-0.1\text{SrTiO}_3-x\text{La}(\text{Mg}_{1/2}\text{Ti}_{1/2})\text{O}_3$ for $x=0$ and 0.02 .²⁰ The third example is the influence of a ternary compound, $\text{La}(\text{Mg}_{1/2}\text{Ti}_{1/2})\text{O}_3$ (LMT) on a homogeneous electrical microstructure, Figure 6. NaNbO_3 is a prime candidate as a dielectric material as it has one of the highest band gaps, $3.4-3.5 \text{ eV}$ amongst all ferroic oxides. The binary system $0.9\text{NaNbO}_3-0.1\text{SrTiO}_3$ is both electrically resistive and electrically homogeneous based on IS data. It requires temperatures $> 450 \text{ }^\circ\text{C}$ to acquire meaningful data. The total resistivity of the ceramics are $\sim 160 \text{ k}\Omega\text{cm}$ at $530 \text{ }^\circ\text{C}$, Figure 6(a) and there is a single (and overlapping) Debye peak in the $-Z''$, M'' spectra, Figure 6(b), indicating that the total resistivity is associated with the grains (bulk). The Arrhenius plot of the bulk conductivity has $E_a \sim 0.9 \text{ eV}$ which is a value commonly reported for extrinsic conduction in BT and ST-based ceramics, Figure 6(e). In this case, the addition of the ternary compound LMT is primarily to increase the bulk resistivity (or lower the conductivity) by at least one order of magnitude and to increase E_a to

$\sim 1.3 \text{ eV}$, Figure 6(e). It has no influence on the electrical homogeneity, Figure 6(c) and (d). The increase in E_a indicates a clear change in the conduction mechanism but isn't close to intrinsic (band gap) conduction given the band gaps of 3.5 and 3.2 eV for NN and ST, respectively. Possible conduction mechanisms are given in the discussion. Nevertheless, the high IR in these NN-based materials lead to impressive BDS that exceed 500 kV/cm .

Octahedral tilting in ferroic oxides

A) Tilting in perovskites and TTBs

A classification and notation for tilting in perovskites was proposed by Glazer⁴⁶ who described tilting as component rotations about the three orthogonal axes. a , b and c denoted the magnitude of each tilt about the $[100]$, $[010]$ and $[001]$ axes of a nominally doubled simple cubic cell. If tilting occurs equally about the axes, this is denoted by repeating the letter, such that 'aaa' refers to equal tilts and 'abc' unequal tilts about each axis. Tilting in-phase and in anti-phase around each axis is described with a superscript '+

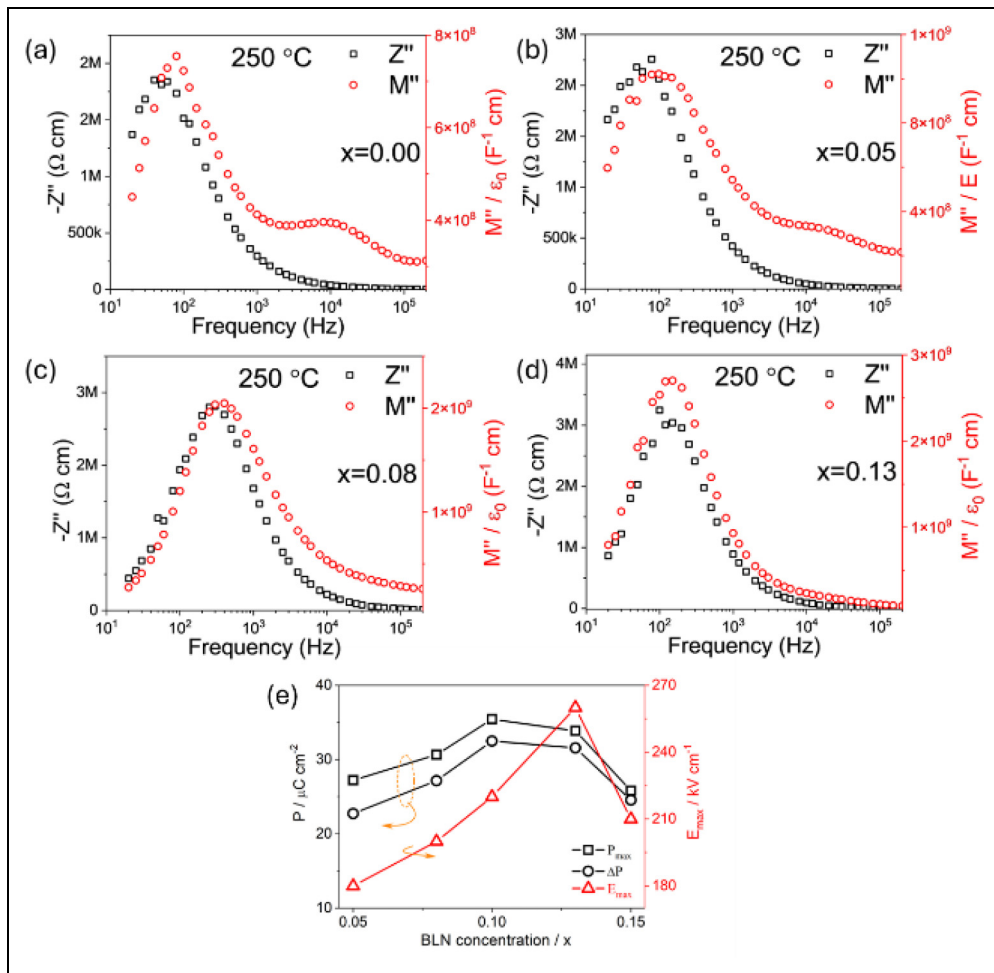


Figure 5. The influence of BLN on the electrical properties of $(0.7 - x)\text{BiFeO}_3\text{-}0.3\text{BaTiO}_3\text{-}x\text{Bi}(\text{Li}_{1/2}\text{Nb}_{1/2})\text{O}_3$ ceramics. $-\text{Z}''$, M'' spectra for $x = 0$ (a), 0.05 (b), 0.08 (c) and 0.13 (d) at 250 °C. P_{max} and E_{max} versus xBLN from P-E loops (e). Figure adapted from ref Wang et al.⁷

or ‘-’, respectively. The absence of tilt around a given axis is relayed by using the superscript ‘0’. $a^-a^-c^+$ therefore refers to a perovskite with antiphase tilting about the pseudocubic a and b axes and in-phase around c , Figure 7. If a structure such as the AFE P phase in NaNbO_3 has a complex or compound tilt around a given axis, a mixed superscript notation is applied, $-/-+$, to give $a^-a^-c^{+/-}$ which indicates that the c -axis, has alternating sets of two in-phase tilted octahedra rotated in antiphase, Figure 8.⁴⁶

For tetragonal tungsten bronzes, tilt configurations are influenced by the non-orthogonal bonding in parts of the octahedral network in contrast to perovskites in which the prototype bonding is orthogonal, Figure 9, creating trigonal, square and pentagonal sites in a [001] projection.⁴⁷ The known octahedral tilted supercells are complex (Figure 10) with many exhibiting incommensurate superstructure.⁴³ Commensurate superstructures are observed for compounds in which the A1-cation is too small for the cuboctahedral volume (square site) with $\text{Sr}_4\text{Na}_2\text{Nb}_{10}\text{O}_{30}$ exhibiting the largest reported superstructure.⁴⁷

A cornerstone of the following examples and the following discussion is the concept of octahedral tilt disorder or frustration. In the context of this article, octahedral tilt disorder/frustration is defined as local changes in the amplitude and/or type of octahedral tilt rotation on a nanoscale.

B) Worked examples of frustrated octahedral tilt systems

Quasi linear dielectric NaNbO_3 based ceramics²⁰. Recently, NaNbO_3 has attracted attention for the development of ceramics for high energy density capacitors due to its large band gap and therefore high intrinsic BDS. In a recent study by Wang et al.,²⁰ NaNbO_3 (AFE, P phase) was initially modified with SrTiO_3 ($0.9\text{NaNbO}_3 - 0.1\text{SrTiO}_3$, NN-ST) which resulted in stabilisation of the FE Q phase which is polar but has the same octahedral tilt structure as CaTiO_3 (Figure 7). Compositions were subsequently modified through the addition of third perovskite member ($0.88\text{NaNbO}_3 - 0.1\text{SrTiO}_3 - 0.02\text{LaMg}_{1/2}\text{Ti}_{1/2}\text{O}_3$, NN-ST-LMT) to reduce the scale length of polar order to give a relaxor phase.²⁰ Finally, polar order was further constrained through the partial substitution of Ta for Nb ($0.88\text{NaNb}_{0.9}\text{Ta}_{0.1}\text{O}_3 - 0.1\text{SrTiO}_3 - 0.02\text{LaMg}_{1/2}\text{Ti}_{1/2}\text{O}_3$ (NNTa_{0.1}-ST-LMT) which resulted in a near linear polarisation field loop and a room temperature paraelectric or quantum paraelectric state at RT. The compositional changes resulted in a decrease in the scale length of polar order from FE to REF to QLD but with a negligible change in perovskite in tolerance factor (t)

$$t = \frac{r_A + r_O}{\sqrt{2}(r_B + r_O)}$$

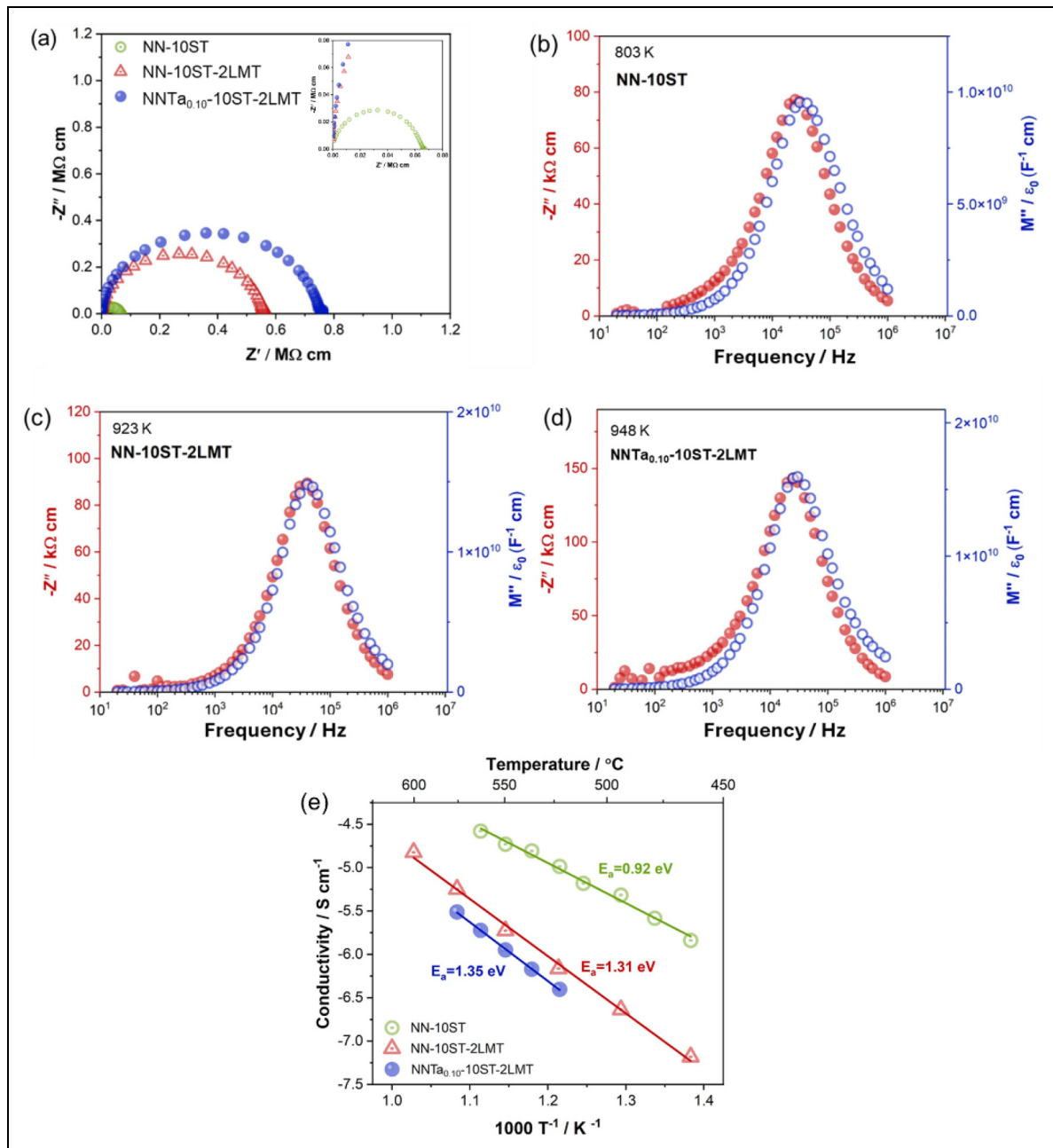


Figure 6. Z^* plots and $-Z''$, M'' spectra for $(0.9-x)\text{NaNbO}_3-0.1\text{SrTiO}_3-x\text{La}(\text{Mg}_{1/2}\text{Ti}_{1/2})\text{O}_3$ for $x=0$ at 803 K (a,b) and 0.02 at 923 K (a,c). Impedance data for the QLD material $0.88[\text{Na}(\text{Nb}_{0.9}\text{Ta}_{0.1})\text{O}_3]-0.10\text{SrTiO}_3-0.02\text{La}(\text{Mg}_{1/2}\text{Ti}_{1/2})\text{O}_3$ at 948 K is included for comparison (a,d). Arrhenius plots of bulk conductivity for all three ceramics (e). Figures adapted from ref Wang et al.²⁰

where r_A , r_B and r_O are average ionic radii of the A-, B- and O-ions, respectively. Across the 3 compositions t remained ~ 0.96 and therefore the structures exhibited a macroscopic $a^-a^-c^+$ tilt system.²⁰

Q-NN MLCCs fabricated using Pt internal electrodes gave rise to exceptional E_{\max} (>2000 kV/cm), energy density (>40 J/cm³), temperature stability matching several EIA criteria that could operate at >200 °C and 10^6 cycles at 1500 kV/cm, Figure 11.²⁰ The authors of ref Sarkar et al.¹⁶ postulated that frustration related to competing structural phase transitions (anti-polar/polar/octahedral tilting) inhibits cooperative displacements from unit cell to unit cell. The absence of cooperative polar displacements ensures that a conventional domain structure does not occur (even under high field) and therefore cooperative switching,

typically observed in FE (microdomains) and REL (nano-domain) phases (Figure 1) is absent, preventing saturation in P-E loops. The complex solid solution also, as discussed, in the worked examples in section 2, also promotes a large BDS.

Further evidence for octahedral tilt frustration, above that shown in ref Wang et al.²⁰, is presented in Figure 12 which shows $<001>$ zone axis diffraction patterns from a NNTa_{0.1}-ST-LMT ceramic with 4 distinct regions of a grain, exhibiting P phase, Q phase and two types of incommensurate structure as evidenced by streaking in the [010] direction. The incommensurate superstructure is attributed to tilt disorder arising from frustration between the 4xP and 2xQ phase. The two images in Figure 12 demonstrate at a microscopic level how the reciprocal space superstructures in the

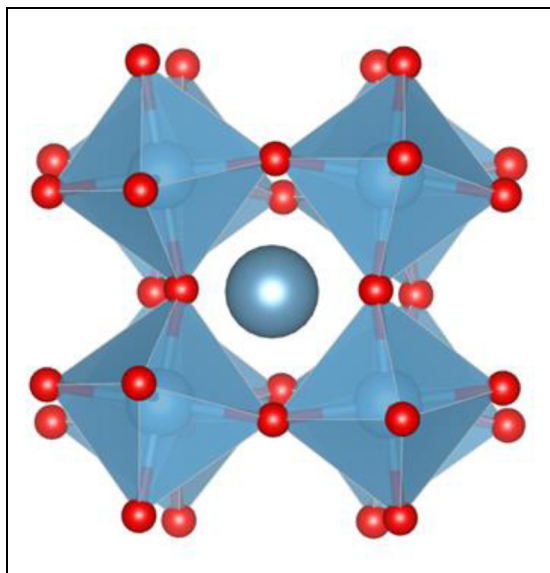


Figure 7. Crystal structure of the fundamental cell of CaTiO_3 which has an $a^-a^-c^+$ glazer tilt⁴⁶ system.

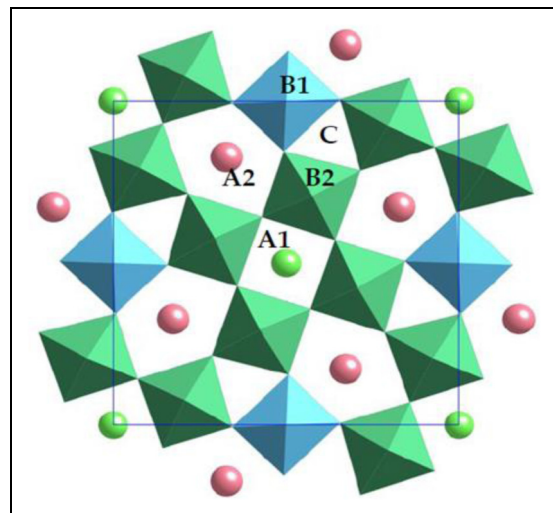


Figure 9. [001] projection of the octahedral framework (B1, B2) of the tetragonal tungsten bronze structure showing trigonal (C), square (A1) and pentagonal (A2) sites. Figure adapted from ref Zhu et al.⁴⁷

diffraction patterns appear as disordered features and defects in real space, consistent with the above arguments.

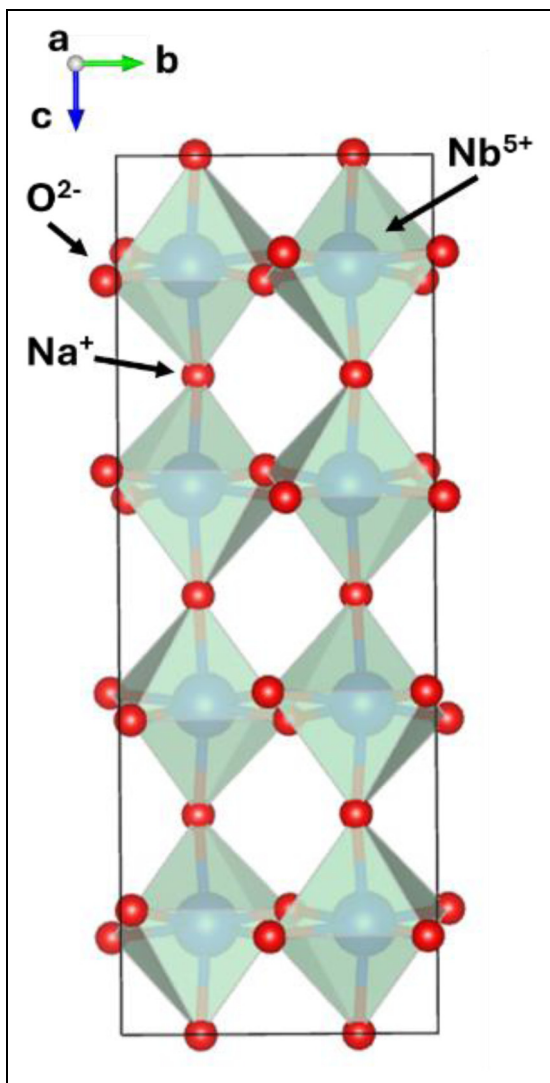


Figure 8. Structure of the P phase of NaNbO_3 in which the octahedral framework ($a^-a^-c^+$) has a $\sqrt{2}a$, $\sqrt{2}a$, $4a$ cell where a is the lattice parameter of the fundamental cubic cell.

Short-range ordered tilting in the $\text{Na}_{1/2}\text{Bi}_{1/2}\text{TiO}_3$ weakly coupled relaxors²¹. The unipolar P-E loops for NBT-SBT-xBMN ceramics at the maximum applied electric field (E_{\max}) are shown in Figure 13. Both W_{rec} and η are significantly enhanced with an increase in BMN concentration, with a maximum W_{rec} of $\sim 7.5 \text{ J/cm}^3$ achieved at $x = 0.08$. Along with the large E_{\max} , resulting from improved resistivity and electrical homogeneity, a large ΔP ($\sim 46 \mu\text{C}/\text{cm}^2$, large $P_{\max} \sim 48 \mu\text{C}/\text{cm}^2$ and small $P_r \sim 1.5 \mu\text{C}/\text{cm}^2$ contribute to the W_{rec} and η , effectively describing an ideal ultra-slim P-E loops (Figure 12(d)) which does not fully saturate as field increases.²¹ Figure 14 shows *in-situ* dark-field, two-beam superlattice TEM images obtained as a function of temperature using $\frac{1}{2}\{hk0\}$ in-phase tilt reflections and the accompanying [001] selected area electron diffraction patterns for $x = 0.08$ recorded at RT. Also included in Figure 14 is a $\langle 110 \rangle$ zone axis diffraction pattern which reveals $\frac{1}{2}\{hkl\}$ superstructure reflections, arising from antiphase tilting, but the absence of $\frac{1}{2}\{hk0\}$. For $\langle 110 \rangle$ zone axes, although reflections of the general type $\frac{1}{2}\{hk0\}$ reflections are permitted, the Weiss Zone Law dictates an extra condition such that $h = k$. For in-phase tilt reflections, $h \neq k$ and are therefore, forbidden in the $\langle 110 \rangle$.²¹ For perovskites with $t < 0.98$, (NBT-SBT-0.08BMNN), combinations of in-phase and antiphase rotations are predicted based on geometric arguments by Glazer⁴² and Reaney et al.⁴⁸ The most likely explanation therefore, for the presence of $\frac{1}{2}\{hk0\}$ and $\frac{1}{2}\{hkl\}$ superstructure reflections in electron diffraction patterns is the coexistence of in-phase and antiphase tilting. Mixed tilt systems which combine in-phase and antiphase rotations are $a^+b^+c^-$, $a^+a^+c^-$, $a^+b^+b^-$, $a^+a^+a^-$, $a^+b^-c^-$, $a^+a^-c^-$, $a^+b^-b^-$, $a+a-a$, $a^0b^-b^+$ and $a^0b^-c^+$. Howard and Stokes⁴⁹ utilised group theory to combine polar displacements with mixed tilting and established 11 possible space groups, $\text{Ama}2$, $\text{Amm}2$, $\text{Cmc}2_1$, Cc , $\text{P}4_2\text{mc}$, $\text{Aba}2$, $\text{Pna}2_1$, $\text{Pmc}2_1$, $\text{Pmn}2_1$, Pc , $\text{P}2_1$ and Pm which

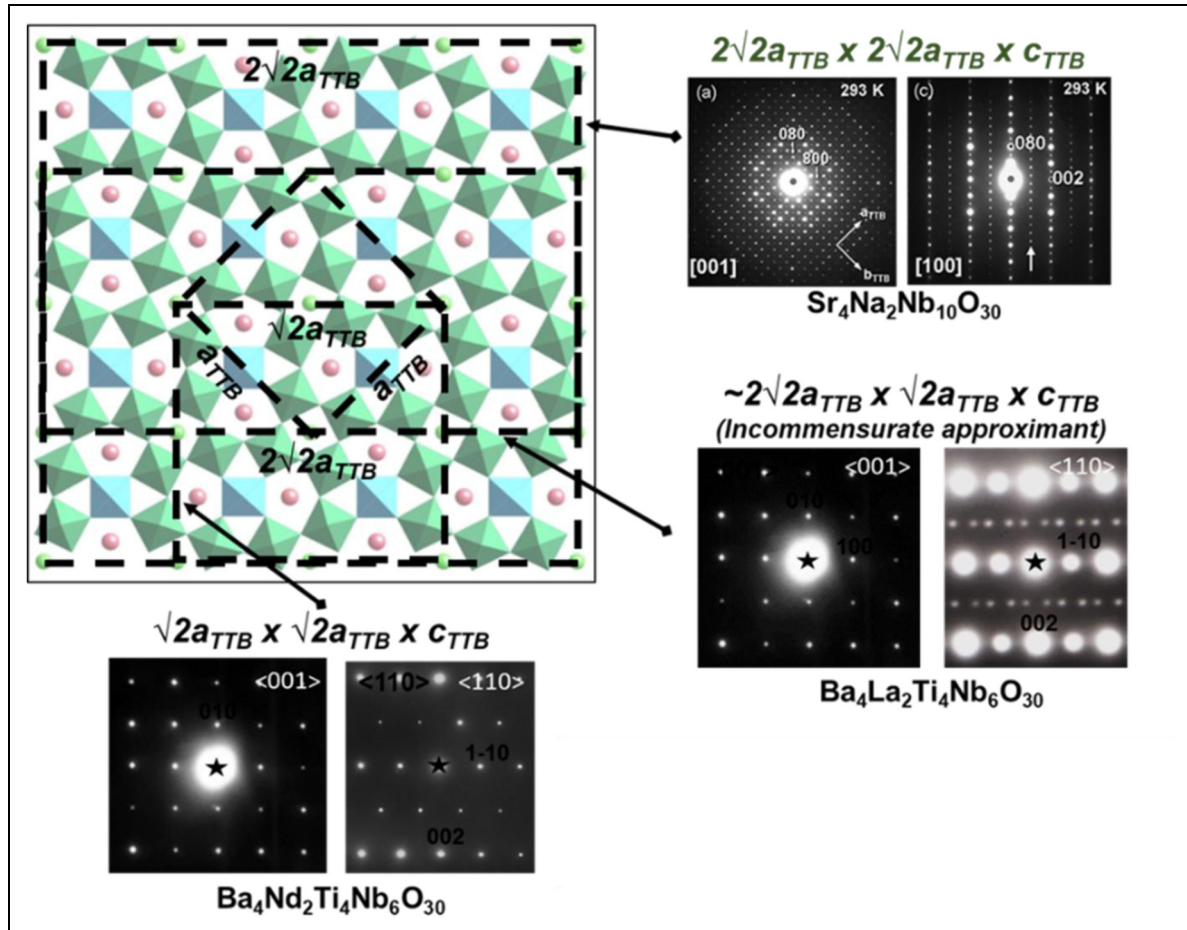


Figure 10. Octahedral tilt supercells in TTB structured ceramics.

therefore, describe the possible local polar structure in NBT-SBT-0.08BMN, all of which are either tetragonal (T), monoclinic (M) or orthorhombic (O). This complex local symmetry creates frustration and disorder above that associated uniquely with the distribution of cations through the perovskite lattice. The effect on the P-E curve is to, not only induce a slim relaxor response, but also to increasingly inhibit saturation, in a manner reminiscent of that observed for Q-NN ceramics²⁰ which also have multiple hierarchies of disorder. Once again, the correct choice of doping and alloying substitutions simultaneously induces a frustrated octahedral tilted and point defect state that favour high energy density through a combination of a high BDS accompanied by limited saturation of the P-E loop. These methodologies for weakly coupled relaxors have been repeated in a large number of systems in which a lower tolerance factor end member has been introduced into a relaxor system, many of which are described in ref Wang et al.⁸.

Nb-based tetragonal tungsten bronze structured ceramics⁵⁰. The authors of ref Duan et al.⁵⁰ substituted Na^+ , Ca^{2+} , Bi^{3+} (A1/A2-sites) and Ta^{5+} (B-site) to induce structural frustration within $(\text{Sr}_{1/2}\text{Ba}_{1/2})_2\text{Nb}_5\text{O}_{15}$ (SBN-H) TTB structured ceramics. They reported disruption to long-range ferroelectric order due to compositional fluctuations which created polar nanoregions (PNRs). They proposed that the high entropy (disorder) in the system reduced the domain-switching energy barriers and weakened domain intercoupling. They achieved a large W_{rec}

of $\approx 10.6 \text{ J cm}^{-3}$ and ultrahigh $\eta \approx 96.2\%$ at 760 kV cm^{-1} and suggested that there was a commensurate improvement in mechanical properties, Figure 15.⁵⁰

Although there is significant disorder in the system, there is no evidence of enhanced solid solution based on a high entropy effect alluded to by the authors of ref Duan et al.⁵⁰, since all dopant ions are known to substitute onto the A1/A2 and B1/B2-sites, based on other TTB structured ceramics.⁴⁷ However, there is no doubt that they have achieved exceptional values of W_{rec} and η . Most strikingly, the almost linear behaviour of the P-E loop is similar to the QLD perovskites reported by ref Wang et al.²⁰ with a large E_{max} (high BDS). In TTB structured ceramics, there is already intrinsic disorder based on frustration between the Nb displacements within the B1 and B2 sites with a general trend towards relaxor behaviour which is only overcome (i.e., when FE order dominates) if there is a large average A1/A2 site ionic radius or through a change in the octahedral tilt framework when there is a small A2 site ion.⁴⁷ The authors of ref Duan et al.⁵⁰ do not consider the octahedral framework in their argument. Based on previous studies in ref Zhu et al.⁴⁷, 'high entropy' TTBs will have an incommensurate superstructure consistent with the Labbe approximant (Figure 10). Therefore, we propose an alternative perspective/explanation to describe their exceptional dielectric behaviour; tilt disorder further limits polar coupling at high field resulting in quasi-linear P-E behaviour similar to NBT²¹ and NN²⁰ based ceramics, in part due to intrinsic

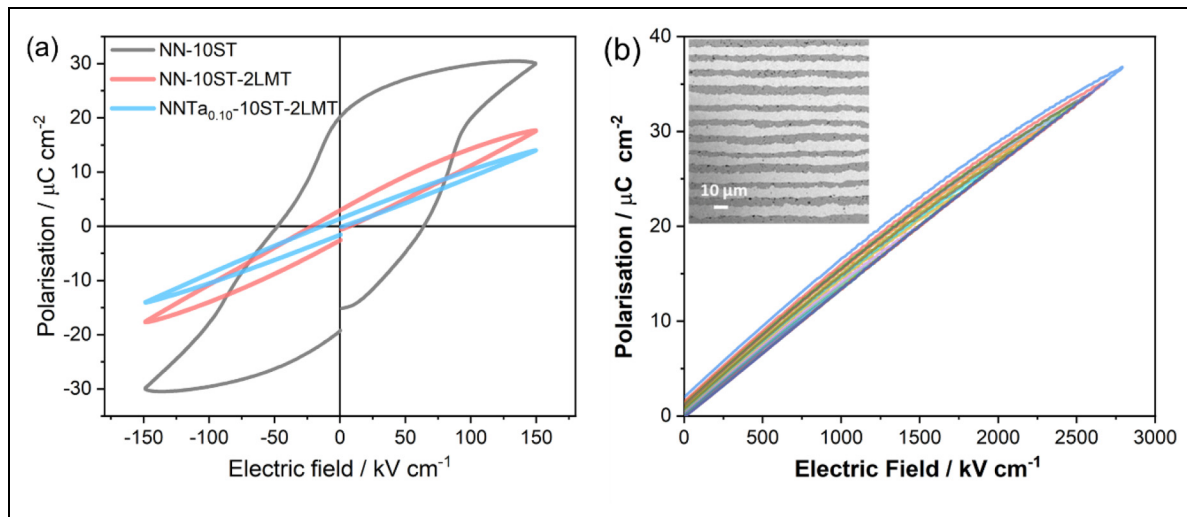


Figure 11. Bulk P-E loops from NN-ST based ceramics and unipolar P-E loop from a Q-NN multilayer. Figure adapted from ref Wang et al.²⁰

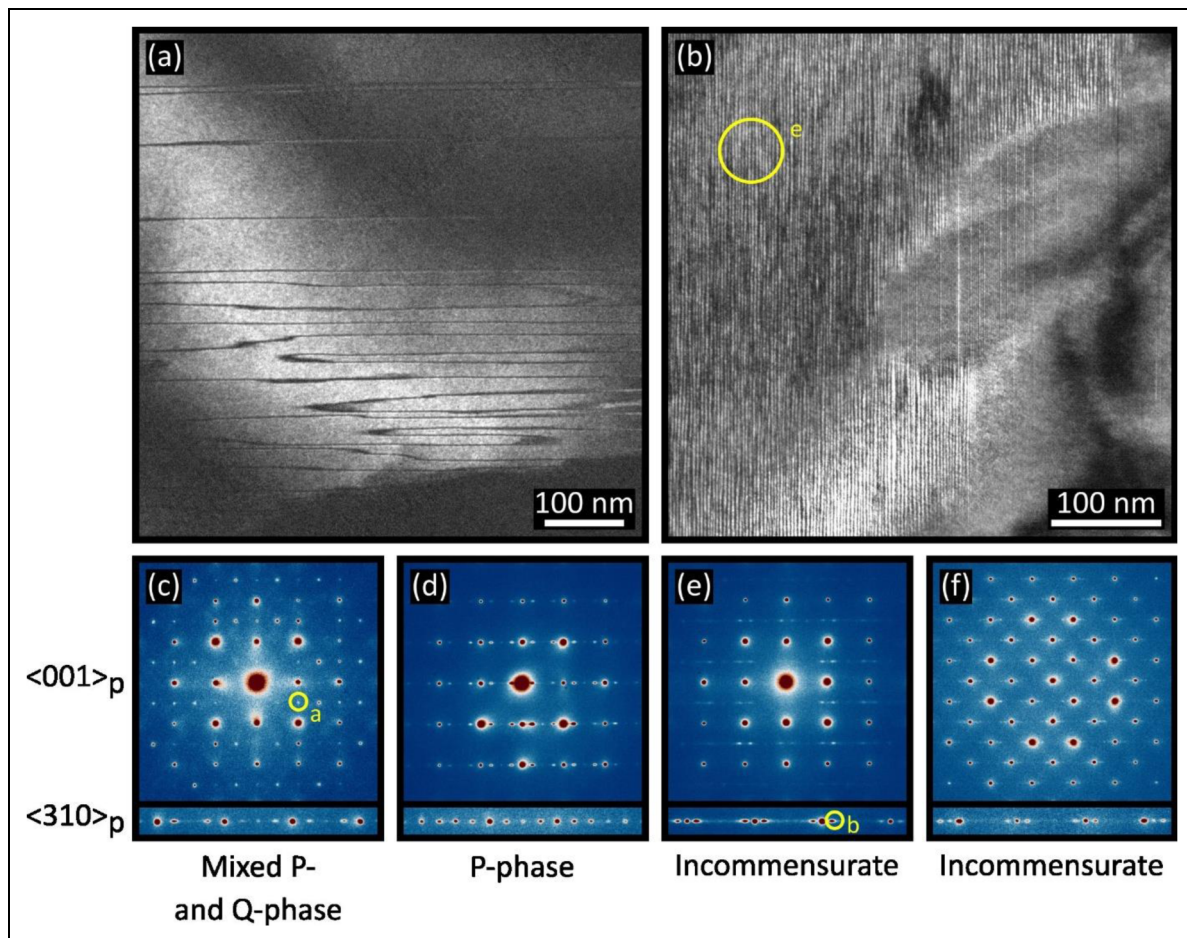


Figure 12. Dark field images from a single grain showing regions of a) antiphase boundaries associated with anti-parallel cation displacements (Q phase) and b) incommensurate superstructure. c-f) $<001>$ zone axis electron diffraction patterns and superstructure reflections in the $<310>$ from different regions of a grain of Q-NN ceramic. The diffraction pattern presented in (e) was recorded from the region indicated in (b) and Dark Field micrographs (a) and (b) were generated by selecting the diffraction spots indicated in (c) and (e), respectively.

incommensurate behaviour but also the ionic radii distribution on the A1/A2 sites. In addition, the 'high entropy' A-site dopants in SBN (Na, Ca and Bi) along with Ta on the B-site create a defect state that enhances BDS. There is

no new physics required to explain the large W_{rec} , only structural frustration which inhibits polarisation saturation, coupled with the ability to apply a large field due to a high BDS.

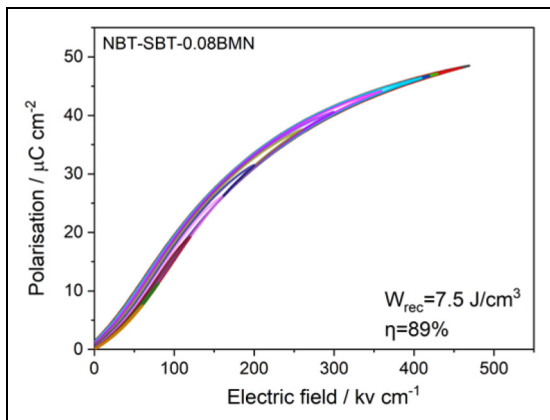


Figure 13. Unipolar P-E loops from NBT-SBT-BMN based ceramics as a function of BMN concentration. Figure adapted from ref Ji et al.²¹

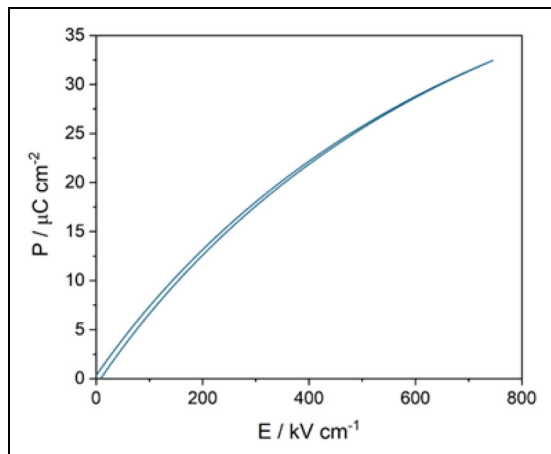


Figure 15. Unipolar P-E loop from SBN-K. Figure adapted from ref Duan et al.⁵⁰

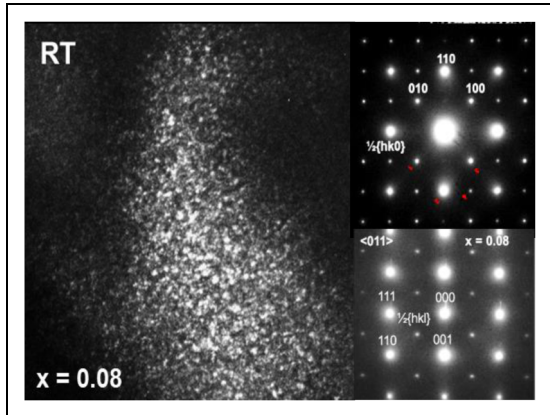


Figure 14. Dark field image show SRO tilted region in NBT based ceramics. $<001>$ and $<110>$ zone axis electron diffraction patterns indicating the presence of octahedral rotation in and out of phase. Figure adapted from ref Ji et al.²¹

Discussion

The work reviewed previously clearly indicates the importance of the defect chemistry and stoichiometric dopants in controlling the breakdown strength (high E_{max}) and also the role of short-range octahedral tilt disorder in creating systems which do not readily saturate at field and which therefore achieve high W_{rec} through increasing E . All thick film (powder) based systems which achieve ultra-high W_{rec} to date correspond to these two criteria which implies that they are key design metrics in optimising high permittivity and voltage MLCCs for power electronics. Key parameters of recent reported materials were summarised in Table 1 below. In the following, we expand upon and discuss the mechanisms by which the conductivity is minimised through the use of stoichiometric dopants and how such dopants in combination with a $t < 1$ matrix create short range ordered tilting which limits the saturation of the P-E loop with increasing E .

A) How short-range tilting suppresses saturation of the P-E loop

In its simplest form saturation of a hysteresis loop in ferroelectrics occurs when all ferroelectric dipoles are aligned

with the direction of the applied electric field. This concept is complicated by microstructural factors such as the grain and domain structure, the multiple orientations of which can limit the direction of the alignment with only a vector of the dipole aligned with the field. Nonetheless, once all the possible re-orientation has occurred, the polarisation is saturated. For imperfect ferroelectrics which exhibit the reorientation of space-charge regions under field, saturation may not be completely achieved as charge may continue to move under the field once the FE-dipoles have reoriented. Since ceramic ferroelectrics all contain space charge regions, a hysteresis loop is often modelled by considering these two types of polarisation with a space-charge hysteresis loop superimposed onto a FE dipolar loop, the relative fractions of which dictate the quality of the FE ceramic.

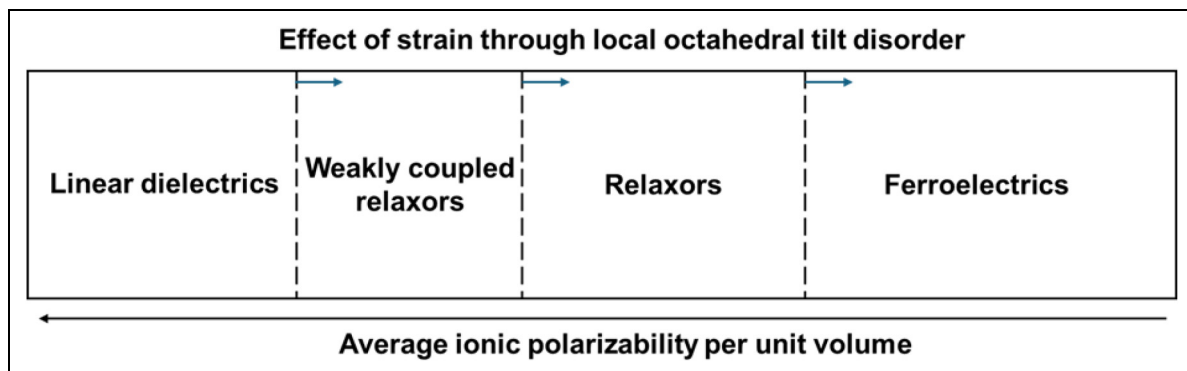
Relaxor ferroelectrics are composed of polar nano regions (PNRs) rather than long range ordered macrodomains, typical of a FE.^{6–12} PNRs can behave in several different ways under large applied fields. Some undergo a relaxor to ferroelectric transition in which the field causes the PNRs to coalesce with the polarisation aligning direction of the applied field, to create long range FE order.⁵⁸ As a result, the P-E loop widens as field increases, commensurate with the extent of PNR coalescence. In weakly coupled relaxors, there is negligible coalescence and the PNRs act largely independently. Their small size ensures that there is minimal energy involved in their reorientation and the loop is slim, even at high field. Nonetheless, there is a finite number of PNRs which when reoriented cause the polarisation to either saturate or tend towards saturation.

Classic linear dielectrics have no polar dipoles to reorientate and charge is stored through mainly ionic polarisation, hence it does not saturate except theoretically under extreme fields well beyond the BDS. Linear dielectrics also are imperfect and reorientation of space-charge defect regions causes the loop to widen, often referred to as a ‘lossy dielectric’. The abiding property of a linear dielectric (class 1) is that it has low permittivity⁴ since there is a negligible re-orientation of charge in comparison with FEs and relaxors.

Despite these text book definitions which are often utilised to explain dipolar behaviour, it is perhaps more instructive to view linear dielectrics,⁴ weakly coupled relaxors,²¹ relaxors^{6–12} and ferroelectrics as 4 regions on a continuum

Table I. Summary of lead-free dielectric ceramics for high energy density ceramic capacitors.

Compositions	W_{rec} / J cm ⁻³	E_{max} / kV cm ⁻¹	η / %	Ref
$[(K_{0.2}Na_{0.8})_{0.8}Li_{0.08}Ba_{0.02}Bi_{0.1}](Nb_{0.68}Sc_{0.02}Hf_{0.08}Zr_{0.1}Ta_{0.08}Sb_{0.04})O_3$	10.1	740	91	Chen et al. ⁵¹
$Sr_{0.35}Ba_{0.35}Na_{0.1}Ca_{0.1}Bi_{0.1}Nb_{1.8}Ta_{0.2}O_6$	10.6	760	96	Duan et al. ⁵⁰
$0.7(Ba_{0.8}Ca_{0.2})TiO_3-0.3Bi(Mg_{0.5}Zr_{0.5})O_3$	10.9	720	93	Kong et al. ⁵²
$BaSrTiNb_{1.9}Ta_{0.1}O_9$	12.2	950	90	Liu et al. ⁵³
0.57BF-0.3BT-0.13Bi(Li _{1/2} Nb _{1/2})O ₃ MLCCs	13.8	950	81	Wang et al. ⁷
0.85NN-0.15 Bi(Ni _{0.5} Hf _{0.5})O ₃ MLCCs	14.1	1215	97	Wang et al. ⁵⁴
0.5BF-0.4ST-0.03Nb-0.1BNM MLCCs	15.8	1000	75	Lu et al. ⁶
(Bi _{2/5} Na _{1/5} K _{1/5} Ba _{1/5})(Ti _{0.7} Hf _{0.3})O ₃	17.2	790	85	Zhu et al. ⁵⁵
0.62NBT-0.3Sr _{0.7} Bi _{0.2} TiO ₃ -0.08BiMg _{2/3} Nb _{1/3} O ₃ MLCCs	18.0	1013	93	Ji et al. ²¹
0.55NBT-0.20NN-0.25ST MLCCs	20.0	1200	87	Li et al. ⁵⁶
(Ba _{0.33} Bi _{0.32} Ca _{0.11} Sm _{0.07} Na _{0.07} Sr _{0.1})(Ti _{0.63} Fe _{0.32} Zr _{0.05})O ₃ MLCCs	20.8	1100	98	Zhang et al. ¹³
0.656NBT-0.144KBT-0.2Sr(S _{0.5} Ta _{0.5})O ₃ MLCCs	23.0	1200	97	Zhao et al. ⁵⁷
0.88NN-0.1ST-0.02La(Mg _{1/2} Ti _{1/2})O ₃ MLCCs	43.5	2800	85	Wang et al. ²⁰

**Figure 16.** Schematic illustrating the scale length of polar order and relevant dielectric behaviour.

along an axis of average ionic polarisability, Figure 16, in which from right to left the degree of saturation decreases. The boundaries between the regions are not distinct and are for illustrative purposes only. They will also depend on factors such as the magnitude of the dipolar displacement in the base material and in the dopants with lone pair electrons (Bi³⁺ and Pb²⁺) typically displacing off-centre in their polyhedral cage more than d⁰ ions (Nb⁵⁺ and Ti⁴⁺). Typically, from right to left there is a marked decrease in the polarisability of the constituent ions which leads to a decrease in ionic displacement, polar coupling and a reduction in permittivity. However, this general principle can be affected by secondary factors such as the amplitude and scale length of octahedral tilting.^{20,21,50} Within a disordered octahedral framework, polarisable ions such as Ti, and Bi can displace off centre, contributing to the permittivity but do not strongly couple to adjacent regions since they have a different tilt configuration (and therefore crystal structure) which frustrates polar coupling and therefore inhibits saturation. When introduced into the diagram the effective linear region is displaced to the right and the permittivity remains far higher than in conventional linear dielectric such as Al₂O₃, resulting in a new class of QLDs.^{20,50}

The advantage of a high permittivity linear material is that the polarisation continues to increase with field, giving rise to a greater area to the left of the P-E loop as E increases and therefore ever greater energy density. The absence of saturation therefore has tremendous benefit for energy density,

provided the material does not break down. To maximise energy density therefore, it is important to have $t < 1$ for the perovskite matrix so that the systems are distorted through octahedral tilting in addition to polar or antipolar behaviour or, as in the case of TTBs, have intrinsic octahedral frustration along with polar behaviour.

One further advantage of QLDs arising from local frustration/competition is the absence of domain switching associated with an FE or a field induced transition typical of many relaxors and antiferroelectrics. Field induced transitions result in a macrodomain state and give rise to large strains. For example, the field induced transition in PbZn_{1/3}Nb_{2/3}O₃-PbTiO₃ ceramics can give rise to up to 0.6% strain⁵⁹ which in an MLCC geometry, this would lead to fracture at the grain boundaries and delamination at the metal ceramic interface under cycling. In contrast even at extreme fields, the strain of the NN-based QLD materials in ref Wang et al.²⁰ does not exceed 0.1% which is much less than a typical PZT (0.2%)⁶⁰ and may be accommodated within the multilayer structure.

In summary, the dopants/alloying substitutions must not only induce local perturbations in the crystal structure and limit strain but also enhance BDS. Fortunately, $t < 1$ matrix materials (e.g., BF, NN, NBT) are common and there is a wide choice of dopants and alloying additions that can maintain $t < 1$ with many cations having the necessary size and valence to frustrate field induced behaviour and enhance IR and BDS in the manner discussed below.

B) Influence of multiple site occupancies on IR and BDS

Three IS examples from the complex perovskite systems described in section 2 illustrate how multiple ion site occupancies can be used to enhance IR and/or BDS of electro ceramics based on changes in the electrical heterogeneity and/or in the predominant conduction mechanism(s). At the outset it is worth noting that ABO_3 is an average composition and that heterogeneity on a local scale exists where the A/B stoichiometry can deviate from =1 and/or local oxygen content is <3 . In all of our examples, intrinsic electronic conduction is never fully achieved and the contribution(s) from ionic conduction, and in particular residual oxygen vacancies (or possibly Na vacancies in the case of NaNbO_3) play a significant role in the conduction mechanisms, either directly or indirectly. Although the measured bulk conductivity by IS may be dominated by either electronic or ionic conduction, a framework based on mixed ionic-electronic conduction, is often a better reference point, as explained below.

- (i) **0.6BiFeO₃-0.4SrTiO₃-xNb where x = 0.00, 0.01, 0.03.**⁶
- (ii) **(0.7 - x)BiFeO₃-0.3BaTiO₃-xBi(Li_{1/2}Nb_{1/2})O₃ for x ≤ 0.13.**⁷
- (iii) **(0.9-x)NaNbO₃-0.1SrTiO₃-xLa(Mg_{1/2}Ti_{1/2})O₃ for x = 0.00 and 0.02.**²⁰

(i) and (ii) are good examples of systems that make use of BiFeO_3 being the major perovskite component (>60 mol%) and given its smaller band gap and higher leakage conduction than $(\text{Ba},\text{Sr})\text{TiO}_3$ -based perovskites the IR of the bulk component in these ceramics is dominated by the defect chemistry of BiFeO_3 and the ceramic processing conditions. In both cases, the inclusion of Nb_2O_5 as a third component, either as additions of Nb_2O_5 (example (i)) or replacement of Fe by Li/Nb on the B-sites (example (ii)) has a significant influence on the bulk conductivity and therefore improvement of IR and/or BDS. In the case of (i), there is a dramatic decrease in bulk conductivity and a change in conduction mechanism, Figure 4(f) with low levels of Nb_2O_5 additions which produces the higher IR. In the case of (ii), IR is not strongly influenced by the Nb-content but it does have a dramatic effect on the electrical homogeneity of the grains, see $-\text{Z}''/\text{M}''$ spectra in Figure 5 which improves the BDS, Figure 5(e). Furthermore, ceramics of x = 0.00 for example (i) [60BF:40ST] were sintered in the range 1070 – 1100 °C with IR ~ 180 k Ω cm at RT, Figure 4(a) whereas for those of x = 0.00 for example (ii) [70BF:30BT] were sintered <1050 °C and IR exceeds ~ 4 M Ω cm at 250 °C, Figure 5(a). This shows the ceramic processing conditions (in the absence of Nb doping/additions) are important and can produce different levels of defects and distribution of ions on a local scale.

In example (i) the lowering of the bulk conductivity by several orders of magnitude and the switch in E_a from ~ 0.4 to ~ 1.2 eV with increasing x can be explained based on the defect chemistry described above for processing of BiFeO_3 -based ceramics with the loss of Bi_2O_3 and B-site donor doping by Nb ions that can compensate for the oxygen vacancies generated. The high bulk conductivity and low E_a

of x = 0.00 is dominated by extrinsic p-type electronic conduction ($\text{Fe}^{3+}/\text{Fe}^{4+}$); however, there are residual oxygen vacancies present and although the ionic contribution to the conductivity (at least in air) is low, it remains present and these ceramics are mixed ionic-electronic conductors. Donor doping with low but sufficient levels of Nb is effective in reducing the level of oxygen vacancies created during sintering and therefore limits the level of oxygen gain on cooling that generates the partial oxidation of Fe^{3+} to Fe^{4+} and therefore suppresses the extrinsic p-type conduction. E_a for the bulk conduction in $x > 0$ ceramics is ~ 1.2 eV which is still below that expected for intrinsic conductivity across the band gap and indicates the bulk conduction mechanism may still include a low-level ionic contribution associated with oxygen vacancies. This is probably unsurprising, as on a local scale there may be some regions of above average acceptor-doping of Sr for Bi on the A-sites beyond the intended, nominal ABO_3 stoichiometry (i.e., $\text{Bi}_{1-x}\text{Sr}_x\text{Fe}_{1-x}\text{Ti}_x\text{O}_3$) based on compensated acceptor (A-site Sr) and donor (B-site Ti) doping of the perovskite lattice and this can create oxygen vacancies (i.e., O <3); however, their mobility and ability to contribute to long range migration is limited to high temperatures/electric fields.

In example (ii), the base binary material (x = 0) contains more BiFeO_3 than in example (i), yet the ceramics are more insulating. The primary reason for this is the lower sintering temperature of ceramics in example (ii) compared to example (i). This produces less Bi_2O_3 loss which creates less oxygen vacancies on sintering and therefore lower levels of oxygen gain on cooling and therefore less partial oxidation of Fe^{3+} to Fe^{4+} to create the high bulk conductivity observed for x = 0 in example (i). However, it is noteworthy that there is clear evidence of electrical heterogeneity in the bulk component of example (ii), see M'' spectra in Figure 5(a); and that the smaller M'' peak at higher frequencies is consistent with leaky p-type regions associated with partial $\text{Fe}^{3+}/\text{Fe}^{4+}$ electronic conduction. These conductive regions are detrimental to BDS and, as in example (i) an increasing amount of Nb via the third perovskite component permits an increasing level of Nb-donor doping (via ionic compensation, i.e., oxide ions as opposed to electronic compensation) that is effective in suppressing this conduction mechanism and results in the grains becoming increasingly electrically homogeneous, see M'' spectra in Figure 5(c) and (d) and the improvement in the dielectric behaviour is reflected in an increase in the BDS for $x > 0.05$ without any significant change in the grain size, Figure 5(e).

In case (iii), NaNbO_3 is the major component of the solid solution and therefore dominates the electrical conduction properties. There is little literature and knowledge on the defect chemistry and the influence of acceptor and donor dopants on the bulk conductivity of NN and other I-V perovskites (e.g., KNbO_3) compared to many II-IV (e.g., SrTiO_3 , BaTiO_3) and III-III (e.g., LaGaO_3) perovskites. In this case, there is a potential issue with volatilisation of Na_2O during ceramic processing which can induce Na and O vacancies which may lead to either or both cation (Na) and/or anion (O) conduction in addition to any electronic conduction. It should be stressed that undoped NN ceramics are generally more resistive than BF based ceramics not only due to the higher band gap but also because there are no

oxidisable cations in NN and any gain in oxygen on cooling from the filling of oxygen vacancies cannot generate the leaky, low E_a p-type semiconductivity observed in BF-systems where Fe^{3+} can be oxidised to Fe^{4+} . Any oxygen gain has to result in partial oxidation of the anion, i.e., O^{2-} to O^- and this generally gives rise to a low level of p-type extrinsic conductivity along with the presence of oxygen vacancies. This type of mixed conduction is also observed in other dielectric perovskites such as undoped BaTiO_3 and SrTiO_3 with E_a typically $\sim 0.8\text{--}0.9$ eV.^{26,27}

Undoped NN has limited A/B non-stoichiometry but this doesn't lead to the same dramatic switch from electronically insulating to high oxide ion conductivity as observed for NBT. The changes are more modest with NN retaining good dielectric behaviour up to ~ 400 °C⁶¹ but there have been reports of undoped NN prepared by Spark Plasma Sintering (SPS) being predominantly a Na ion conductor.⁶² For dopant studies, there are reports of acceptor-type Ti-doping on the B-site (again by SPS) inducing O vacancies and increasing the level of oxide ion conductivity,⁶² whereas donor-type Sr-doping on the A-site induces A-site vacancies with only modest changes in the bulk conductivity.⁶³ In the former case, the doping limit is ~ 5 at% whereas in the latter it is ~ 20 at% and these results suggest that oxygen vacancy migration is more facile in NN than Na ion migration but further studies with a wider range of dopants are required to substantiate this hypothesis.

For nominally stoichiometric $x=0$ in example (iii) the bulk conductivity is low until > 400 °C and the associated E_a is consistent with that described above for mixed ionic-electronic conduction. The inclusion of the third perovskite does not influence the electrical homogeneity based on $-Z''$, M'' spectra, Figure 6(b)–(d) but has a significant effect in reducing the bulk conductivity, increasing both IR and the associated E_a , Figure 6(e). If the donor-acceptor compensated mechanism of $\text{La}(\text{Mg}_{1/2}\text{Ti}_{1/2})\text{O}_3^{20}$ is consistent on a local scale then no new defects are created and only a small (if any) change to the band gap would be expected for such a low level of the third component. Therefore, no significant changes in bulk conductivity would be expected. Based on the limited available information on the defect chemistry of NaNbO_3 , the influence of individual ions that might occur locally on the A and B-sites of NN would be creation of A-site vacancies on La (donor) doping and oxygen vacancies on Mg, Ti (acceptor) doping, respectively; however, these are unlikely to contribute to long range migration.

The most plausible explanation for the suppression of the conductivity is the creation of deep potential energy wells in the saddle points (i.e., bottlenecks) associated with the oxide-ion migration pathway between two A-sites and a B-site ion in the perovskite lattice, Figure 3. The addition of the third component (ignoring Ta in the optimised QLD material) results in a distribution of three different sized A-site [Na (1.39 Å), Sr (1.42 Å) and La (1.36 Å)] and B-site cations [Nb (0.64 Å), Mg (0.72 Å) and Ti (0.605 Å)] which creates localised strain linked to the octahedral tilting networks. This variance in cation size, mass, polarisability and bond strength to oxygen on a local scale suppresses the long-range migration of oxide ions and reduces the level of ionic conduction in these materials, both in terms of carrier concentration (n) and mobility (μ), given $\sigma = nq\mu$ where q is the charge on the carrier. This

leads to materials where the ionic contribution to the mixed bulk conductivity is heavily suppressed, but it is interesting to note that the E_a of ~ 1.3 eV is substantially less than that expected for intrinsic electronic conduction. This indicates the bulk conduction mechanism(s) in these ternary based materials to be complex and worthy of further investigation. What is clear, is there are no significant donor or acceptor electronic doping mechanisms that give rise to high levels of n- or p-type (electronic) semiconductivity with low E_a (i.e. < 0.4 eV) in these NN-based materials.

The variance in mass of the multiple cations and their different bond strengths to oxygen influence the local vibrations (and therefore phonons) that contribute to the mobility of both the electronic and ionic conduction carriers in these materials. This influences both the measured electrical and thermal conductivity in these materials and may not only increase IR but also reduce self-heating and thermal runaway. Further studies are required but a phonon-glass approach using multiple cations and vacancies in perovskite and TTB lattices is a well-established mechanism in lowering thermal conductivity in thermoelectric oxides.⁶⁴ Although it is beyond the scope of this script, future studies should investigate both the electrical and thermal conduction mechanisms in these materials to ensure optimisation in suppressing IR and thermal runaway whilst maximising BDS.

Conclusions and future directions

In this script we demonstrate two key design metrics in multi-valent polar/anti polar perovskites (with $t < 1$) and polar TTBs (with intrinsic octahedral frustration) to optimise high permittivity and voltage MLCCs for power electronics. First, the importance of controlling the defect chemistry and stoichiometric dopants in the perovskite materials to achieve homogeneous electrical microstructures to maximise the IR and BDS (high E_{\max}). Second, the role of short-range octahedral tilt disorder in creating systems which do not readily saturate with electric field and which therefore achieve high W_{rec} through increasing E . Furthermore, we propose a synergistic effect between these two metrics as the local compositional disorder that creates the short-range octahedral disorder and lattice strain is effective in suppressing ionic conductivity (predominantly oxide ions) at high electric fields. As a consequence, the short range ordered tilting that produces quasi linear P-E behaviour can be exploited to higher E by high IR and enhanced BDS.

A key feature of this work is how (nominally stoichiometric) compositional change can decrease the scale length of polar disorder without significant changes in the average tolerance factor of the materials. The presence of mixed tilt systems with complex local symmetry creates frustration and disorder above that associated uniquely with the distribution of the cations through the perovskite/TTB lattice. We argue that the variance in the size and mass of the multiple cations and their different bond strengths to oxygen create the necessary strain to produce the desired quasi linear dielectric properties for high energy density applications. Coincidentally, such situations often occur in multicomponent so-called 'high entropy' systems but invoking 'entropy' arguments does not attest to the underpinning crystal chemistry which leads high energy density/voltage dielectrics.

Future directions in high energy density ceramics are numerous and span from improved fundamental understanding, design and characterisation of QLD complex oxides to achieving materials that are compatible with existing BME MLCCs technology for scale-up of commercial applications. For materials development there is need to employ advanced characterisation methods to establish the local compositional and structural disorder in QLD perovskite/TTB oxides to garner better insight as to how they link with the electrical properties to inform on future design(s) to achieve optimisation. Given the importance of cation and anion displacements and octahedral tilting in these QLD materials, its imperative that techniques that can characterise both cation and anion sublattices on a local scale for dipolar mapping be employed. Good recent examples of this on NaNbO_3 -based materials are the use of total scattering methods^{65,66} and electron ptychography.⁶⁷ In addition, computational methods such as phase field simulations are becoming invaluable for understanding the evolution of polar domain structures as solid solutions are formed between two or more materials. For example, in the NaNbO_3 - $\text{Bi}(\text{Ni}_{1/2}\text{Hf}_{1/2})\text{O}_3$ system the long range ordered NaNbO_3 AFE microdomains are broken into nanodomains embedded in a polar orthorhombic matrix with a certain orientation with increasing $\text{Bi}(\text{Ni}_{1/2}\text{Hf}_{1/2})\text{O}_3$ content.⁵⁴ It is clear that a combination of advanced experimental and computational methods is going to be required to answer many of the remaining scientific questions in the development of these more complex QLD materials. For example, what are the upper and lower limits to the polar disorder in these complex perovskite/TTB systems to achieve QLD and is there an upper limit to the permittivity that can be achieved? Can these QLD materials achieve the high permittivity (> 1000) values obtained in conventional FE and RFE?

ORCID iDs

Robin Sjökvist  <https://orcid.org/0000-0001-5571-2986>
Ge Wang  <https://orcid.org/0000-0003-1842-8067>

Author contributions

Ian M. Reaney: Conceptualisation, Methodology, Investigation, Data Analysis, Writing-Original Draft, Writing-Review & Editing, Supervision
Richard Beanland: Methodology, Investigation, Data Analysis, Writing-Review & Editing
Robin Sjökvist: Methodology, Investigation, Data Analysis, Writing-Review & Editing
Yubo Zhu: Methodology, Investigation, Data Analysis
Ge Wang: Methodology, Investigation, Data Analysis, Writing-Review & Editing
Derek C. Sinclair: Conceptualisation, Methodology, Investigation, Data Analysis, Writing-Review & Editing, Supervision

Funding

The authors disclosed receipt of the following financial support for the research, authorship, and/or publication of this article: This work was supported by the Engineering and Physical Sciences Research Council, (grant number EP/Z536003/1). Ge Wang would like to acknowledge the financial support from Dame Kathleen Ollerenshaw Fellowship provided by The University of Manchester.

Declaration of conflicting interests

The authors declared no potential conflicts of interest with respect to the research, authorship, and/or publication of this article.

References

1. Baliga BJ. *Wide bandgap semiconductor power devices*. UK: Woodhead Publishing, 2019.
2. Wang G, Li J, Zhang X, et al. Ultrahigh energy storage density lead-free multilayers by controlled electrical homogeneity. *Energy Environ Sci* 2019; 12: 582–588.
3. Randall CA, Fan Z, Reaney IM, et al. Antiferroelectrics: history, fundamentals, crystal chemistry, crystal structures, size effects, and applications. *J Am Ceram Soc* 2021; 104: 3775–3810.
4. <https://www.doeet.com/content/eee-components/passives/class-1-ceramic-dielectrics/>
5. Telmer RM, Hilario SM, Hoff WB, et al. Anisotropy of W-band complex permittivity in Al_2O_3 . *J Phys: Condens Matter* 2019; 31: 225702.
6. Lu Z, Wang G, Bao W, et al. Superior energy density through tailored dopant strategies in multilayer ceramic capacitors. *Energy Environ Sci* 2020; 13: 2938–2948.
7. Wang G, Lu Z, Yang H, et al. Fatigue resistant lead-free multilayer ceramic capacitors with ultrahigh energy density. *J Mater Chem A* 2020; 8: 11414–11423.
8. Wang G, Lu Z, Li Y, et al. Electroceramics for high-energy density capacitors: current status and future perspectives. *Chem Rev* 2021; 121: 6124–6172.
9. Yang H, Lu Z, Li L, et al. Novel BaTiO_3 -Based, Ag/Pd-compatible lead-free relaxors with superior energy storage performance. *ACS Appl Mater Interfaces* 2020; 12: 43942–43949.
10. Wang X, Fan Y, Zhang B, et al. High discharge energy density in novel $\text{K}_{1/2}\text{Bi}_{1/2}\text{TiO}_3$ - BiFeO_3 based relaxor ferroelectrics. *J Euro Ceram Soc* 2022; 42: 7381–7387.
11. Yang H, Bao W, Lu Z, et al. High-energy storage performance in BaTiO_3 -based lead-free multilayer ceramic capacitors. *J Mater Res* 2021; 36: 1285–1294.
12. Zubairi H, Wasim M, Liu Y, et al. High permittivity short-range orthorhombic Q phase in CaTiO_3 modified NaNbO_3 ferroelectric ceramics. *Ceram Inter* 2025; 51: 59862–59867.
13. Zhang M, Lan S, Yang BB, et al. Ultrahigh energy storage in high-entropy ceramic capacitors with polymorphic relaxor phase. *Science* 2024; 384: 185–189.
14. Xi J, Liu J, Bai W, et al. Design of lead-free high-entropy quasi-linear dielectrics with giant comprehensive electrostatic energy storage. *Acta Mater* 2025; 289: 120931.
15. Rost CM, Sachet E, Borman T, et al. Entropy-stabilised oxides. *Nat Commun* 2015; 6: 8485.
16. Sarkar A, Wang Q, Schiele A, et al. High-entropy oxides: fundamental aspects and electrochemical properties. *Adv Funct Mater* 2019; 31: 1806236.
17. Brahlek M, Gazda M, Keppens V, et al. What is in a name: defining ‘high entropy’ oxides. *APL Mater* 2022; 10: 110902.
18. Murakami S, Ahmed NTAF, Wang D, et al. Optimising dopants and properties in BiMeO_3 ($\text{Me} = \text{Al}, \text{Ga}, \text{Sc}, \text{Y}, \text{Mg}_{2/3}\text{Nb}_{1/3}, \text{Zn}_{2/3}\text{Nb}_{1/3}, \text{Zn}_{1/2}\text{Ti}_{1/2}$) lead-free BaTiO_3 - BiFeO_3 based ceramics for actuator applications. *J Eur Ceram Soc* 2018; 38: 4220–4231.
19. Murakami S, Wang D, Mostaed A, et al. High strain (0.4%) $\text{Bi}(\text{Mg}_{2/3}\text{Nb}_{1/3})\text{O}_3$ - BaTiO_3 - BiFeO_3 lead-free piezoelectric

ceramics and multilayers. *J Am Ceram Soc* 2018; 101: 5428–5442.

- 20. Wang X, Song X, Fan Y, et al. Lead-free high permittivity quasi-linear dielectrics for giant energy storage multilayer ceramic capacitors with broad temperature stability. *Adv Energy Mater* 2024; 14: 2400821.
- 21. Ji H, Wang D, Bao W, et al. Ultrahigh energy density in short-range tilted NBT-based lead-free multilayer ceramic capacitors by nanodomain percolation. *Energy Storage Mater* 2021; 38: 113–120.
- 22. Gao Y, Song Z, Hu H, et al. Optimizing high-temperature energy storage in tungsten bronze-structured ceramics via high-entropy strategy and bandgap engineering. *Nat Commun* 2024; 15: 5869.
- 23. Irvine JTS, Sinclair DC and West AR. Electroceramics: characterization by impedance spectroscopy. *Adv Mater* 1990; 2: 132–138.
- 24. Carroll EL, Killeen JH, Feteira A, et al. Influence of electrode contact arrangements on polarisation-electric field measurements of ferroelectric ceramics: a case study of BaTiO₃. *J Materomics* 2025; 11: 100939.
- 25. Hareem Z, Zhilun L, Yubo Z, et al. Current development, optimisation strategies and future perspectives for lead-free dielectric ceramics in high field and high energy density capacitors. *Chem Soc Rev* 2024; 53: 10761–10790.
- 26. Heath JP, Harding JH, Sinclair DC, et al. The analysis of impedance spectra for core-shell microstructures: why a multi-formalism approach is essential. *Adv Funct Mater* 2019; 29: 1904036.
- 27. Chan NH, Sharma RK and Smyth DM. Nonstoichiometry in acceptor-doped BaTiO₃. *J Am Ceram Soc* 1982; 65: 167–170.
- 28. Smyth DM. *The defect chemistry of metal oxides*. USA: Oxford University Press, 2000.
- 29. Buscaglia V and Randall CA. Size and scaling effects in barium titanate. *J Eur Ceram Soc* 2020; 40: 3744–3758.
- 30. Li M, Pietrowski MMJ, De Souza RA, et al. A family of oxide ion conductors based on the ferroelectric perovskite Na_{0.5}Bi_{0.5}TiO₃. *Nat Mater* 2014; 13: 31–35.
- 31. Meyer KC and Albe K. Influence of phase transitions and defect associates on the oxygen migration in the ion conductor Na_{1/2}Bi_{1/2}TiO₃. *J Mater Chem A* 2017; 5: 4368–4375.
- 32. Yang F, Li M, Li L, et al. Defect chemistry and electrical properties of sodium bismuth titanate perovskite. *J Mater Chem A* 2018; 6: 5243–5254.
- 33. Yang F, Hu Y, Hu Q, et al. Dramatic impact of the TiO₂ polymorph on the electrical properties of ‘stoichiometric’ Na_{0.5}Bi_{0.5}TiO₃ ceramics prepared by solid-state reaction. *J Mater Chem A* 2022; 10: 891–901.
- 34. Li M, Zhang H, Cook SN, et al. Dramatic influence of A-site non-stoichiometry on the electrical conductivity and conduction mechanisms in the perovskite oxide Na_{1/2}Bi_{1/2}TiO₃. *Chem Mater* 2015; 27: 629–634.
- 35. He X and Mo Y. Accelerated materials design of Na_{0.5}Bi_{0.5}TiO₃ oxygen ionic conductors based on first principles calculations. *Phys Chem Chem Phys* 2015; 17: 18035–18044.
- 36. Zhang H, Ramadan AHH and De Souza RA. Atomistic simulations of ion migration in sodium bismuth titanate (NBT) materials: towards superior oxide-ion conductors. *J Mater Chem A* 2018; 6: 9116–9123.
- 37. Li L, Kler J, West AR, et al. High oxide-ion conductivity in acceptor-doped Bi-based perovskites at modest doping levels. *Phys Chem Chem Phys* 2021; 23: 11327–11333.
- 38. Li M, Li L, Zang J, et al. Donor-doping and reduced leakage current in Nb-doped Na_{0.5}Bi_{0.5}TiO₃. *Appl Phys Lett* 2015; 106: 102904.
- 39. Masó N and West AR. Electrical properties of Ca-doped BiFeO₃ ceramics: from p-type semiconduction to oxide-ion conduction. *Chem Mater* 2012; 24: 2127–2132.
- 40. Hu W, Liu Y, Withers RL, et al. Electron-pinned defect-dipoles for high performance colossal permittivity materials. *Nat Mater* 2013; 12: 821–826.
- 41. Kakimoto S, Hashimoto Y, Kuwano T, et al. Controlling dielectric properties of Nb + X (X = Al, Ga, In) co-doped and Nb-doped rutile-type TiO₂ single crystals. *J Mater Chem C* 2023; 11: 1304–1310.
- 42. Taniguchi H, Sato D, Nakano A, et al. Permittivity boosting in ‘yellow’ (Nb + In) co-doped rutile ceramics. *J Mater Chem C* 2020; 8: 13627–13631.
- 43. Sinclair DC, Adams TB, Morrison FD, et al. Cacu₃Ti₄O₁₂: a one-step internal barrier layer capacitor. *Appl Phys Lett* 2002; 80: 2153–2155.
- 44. Ferrarelli MC, Sinclair DC, West AR, et al. Comment on the origin(s) of the giant permittivity effect in CaCu₃Ti₄O₁₂ single crystals and ceramics. *J Mater Chem* 2009; 19: 5916–5919.
- 45. Li M, Sinclair DC and West AR. Extrinsic origins of the apparent relaxor-like behavior in CaCu₃Ti₄O₁₂ ceramics at high temperatures: a cautionary tale. *J Appl Phys* 2011; 109: 084106.
- 46. Glazer AM. The classification of tilted octahedra in perovskites. *Acta Crystallogr A* 1972; 28: 3384–3392.
- 47. Zhu X, Fu M, Stennett MC, et al. A crystal-chemical framework for relaxor versus normal ferroelectric behavior in tetragonal tungsten bronzes. *Chem Mater* 2015; 27: 3250–3261.
- 48. Reaney IM, Colla EL and Setter N. Dielectric and structural characteristics of Ba-and Sr-based complex perovskites as a function of tolerance factor. *Jpn J Appl Phys* 1994; 33: 3984.
- 49. Howard CJ and Stokes HT. Group-theoretical analysis of octahedral tilting in perovskites. *Acta Crystallogr Sect B* 1998; 54: 782–789.
- 50. Duan J, Wei K, Du Q, et al. High-entropy tungsten bronzes for large capacitive energy storage with near-zero losses. *Adv Funct Mater* 2024; 34: 2409446.
- 51. Chen L, Deng S, Liu H, et al. Giant energy-storage density with ultrahigh efficiency in lead-free relaxors via high-entropy design. *Nat Commun* 2024; 3: 3089.
- 52. Kong X, Yang L, Meng F, et al. High-entropy engineered BaTiO₃-based ceramic capacitors with greatly enhanced high-temperature energy storage performance. *Nat Commun* 2025; 16: 85.
- 53. Liu J, Jiang Y, Zhang W, et al. Ferroelectric tungsten bronze-based ceramics with high-energy storage performance via weakly coupled relaxor design and grain boundary optimization. *Nat Commun* 2024; 15: 8651.
- 54. Wang Z, Li D, Liu W, et al. Ultra-high energy storage in lead-free NaNbO₃-based relaxor ceramics with directional slush-like polar structure design. *Nat Commun* 2025; 16: 2892.
- 55. Zhu B, Wang X, Zhang J, et al. Designing Pb-free high-entropy relaxor ferroelectrics with machine learning assistance for high energy storage. *J Am Chem Soc* 2025; 147: 27912–27921.
- 56. Li D, Liu Z, Zhao W, et al. Global-optimized energy storage performance in multilayer ferroelectric ceramic capacitors. *Nat Commun* 2025; 16: 88.
- 57. Zhao W, Liu Z, Xu D, et al. Advanced stability and energy storage capacity in hierarchically engineered Bi_{0.5}Na_{0.5}TiO₃-based multilayer capacitors. *Nat Commun* 2025; 16: 6549.

58. Paterson AR, Nagata H, Tan X, et al. Relaxor-ferroelectric transitions: sodium bismuth titanate derivatives. *MRS Bull* 2018; 43: 600–606.
59. Davis M, Damjanovic D and Setter N. Electric-field-, temperature-, and stress-induced phase transitions in relaxor ferroelectric single crystals. *Phys Rev B* 2006; 73: 014115.
60. Hoffmann MJ, Hammer M, Endriss A, et al. Correlation between microstructure, strain behavior, and acoustic emission of soft PZT ceramics. *Acta Mater* 2001; 49: 1301–1310.
61. Ruf T, Mauck M, Mognin C, et al. The influence on sintering and properties of sodium niobate (NaNbO_3) ceramics by “non-stoichiometric” precursor compositions. *Mater Chem Phys* 2019; 229: 437–447.
62. Gouget G, Mauvy F, Chung UC, et al. Associating and tuning sodium and oxygen mixed-ion conduction in niobium-based perovskites. *Adv Funct Mater* 2020; 30: 1909254.
63. Hooper TE and Sinclair DC. Structural, dielectric, and conduction behaviour of A-site deficient $\text{Sr}_x\text{Na}_{1-2x}\text{NbO}_3$ ceramics. *J Mater Chem C* 2024; 12: 12992–13001.
64. Lu Z, Zhang H, Lei W, et al. High-figure-of-merit thermoelectric La-doped A-site-deficient SrTiO_3 ceramics. *Chem Mater* 2016; 28: 925–935.
65. Levin I, Yang F, Maier R, et al. Displacive order-disorder behavior and intrinsic clustering of lattice distortions in Bi-substituted NaNbO_3 . *Adv Funct Mater* 2020; 30: 2001840.
66. Zhang MH, Ding H, Egert S, et al. Tailoring high-energy storage NaNbO_3 -based materials from antiferroelectric to relaxor states. *Nat Commun* 2023; 14: 1525.
67. Harikrishnan KP, Xu R, Patel K, et al. Electron ptychography reveals a ferroelectricity dominated by anion displacements. *Nat Mater* 2025; 24.